Department of Biomedical Engineering and Computational Science

Combined ultra-low-field MRI and MEG: instrumentation and applications

Panu Vesanen

Aalto University

DOCTORAL DISSERTATIONS

Aalto University publication series
DOCTORAL DISSERTATIONS 87/2013

Combined ultra-low-field MRI and MEG: instrumentation and applications

Panu Vesanen

Doctoral dissertation for the degree of Doctor of Science in Techology (Doctor of Philosophy) to be presented with due permission of the School of Science for public examination and debate in Auditorium F239 at the Aalto University School of Science (Espoo, Finland) on the 24th of May 2013 at 12 noon

Aalto University
School of Science
Department of Biomedical Engineering and Computational Science

Supervising professor
Prof. Risto Ilmoniemi

Thesis advisor
Prof. Risto Ilmoniemi

Preliminary examiners
Prof. Alexander Braginski, Forschungszentrum Jülich, Germany
Dr. Gösta Ehnholm, Philips Medical Systems MR Finland, Finland

Opponent
Prof. Jürgen Hennig, University Medical Center Freiburg, Germany

Aalto University publication series
DOCTORAL DISSERTATIONS 87/2013

ISBN 978-952-60-5177-2 (printed)
ISBN 978-952-60-5178-9 (pdf)
ISSN-L 1799-4934
ISSN 1799-4934 (printed)
ISSN 1799-4942 (pdf)
http://urn.fi/URN:ISBN:978-952-60-5178-9

Unigrafia Oy
Helsinki 2013

Finland

441 697
Printed matter

Aalto University

Abstract

Aalto University, P.O. Box 11000, FI-00076 Aalto www.aalto.fi

Author
Panu Vesanen

Name of the doctoral dissertation
Combined ultra-low-field MRI and MEG: instrumentation and applications

Publisher School of Science

Unit Department of Biomedical Engineering and Computational Science

Series Aalto University publication series DOCTORAL DISSERTATIONS 87/2013

Field of research Biomedical Engineering and Biophysics

Manuscript submitted 11 January 2013 **Date of the defence** 24 May 2013

Permission to publish granted (date) 10 April 2013 **Language** English

☐ **Monograph** ☒ **Article dissertation (summary + original articles)**

Abstract

Magnetic resonance imaging (MRI) is a noninvasive method that allows the study of the interior structure of matter. Today, MRI is widely used in medical diagnosis and research, thanks to its versatile contrast and the lack of ionizing radiation. Conventionally, the signal-to-noise ratio of an MRI measurement scales with the strength of the applied magnetic field. This has driven the development of MRI scanners towards fields of 3 T and above.

Ultra-low-field (ULF) MRI is an emerging technology that uses microtesla-range magnetic fields for image formation. The low signal-to-noise ratio is partly compensated for by prepolarizing the sample in a field of 1 – 200 mT and using superconducting quantum interference devices (SQUIDs) for signal detection. Advantages of ULF MRI include unique low-field contrast mechanisms, flexibility in the sequence design, and the possibility to construct a silent scanner with an open geometry. ULF MRI is also compatible with magnetoencephalography (MEG), which uses SQUIDs to record the magnetic field produced by neuronal activity. With a hybrid scanner combining MEG and MRI, both the structure and function of the human brain can be studied with a single device.

In this Thesis, a hybrid MEG-MRI device was designed, constructed, and tested. The system is based on a commercial whole-head MEG device that was modified to accommodate ULF-MRI functionality. In particular, the effects of the various magnetic fields applied inside a magnetically shielded room were studied. To prevent the harmful effects of the eddy currents caused by changing magnetic fields, a self-shielded polarizing coil was designed and constructed. Moreover, the conventional SQUID design was modified in order to develop sensor modules that tolerate the relatively strong polarizing field. Finally, the device was used to measure MEG data and ULF-MR images of the human brain.

In addition to the instrumentation development, several applications of ULF MRI were investigated. A method for imaging electric current density was presented. The technique takes advantage of the flexibility of ULF MRI by encoding the signal in zero magnetic field. Furthermore, the temperature dependence of the MRI relaxation times was studied. Drastic variations were found as a function of the field strength. The results were used to reconstruct temperature maps using ULF MRI.

The results presented in this Thesis demonstrate that upgrading MRI functionality into an existing commercial MEG device is a feasible concept. Such a device has the potential to enable new methods and paradigms for neuroscientific research. The possibility of taking advantage of the unique low-field contrast is an interesting subject for further research.

Keywords Magnetic resonance imaging, MRI, ultra-low-field MRI, magnetoencephalograhy, MEG, MEG-MRI, SQUID

ISBN (printed) 978-952-60-5177-2 **ISBN (pdf)** 978-952-60-5178-9

ISSN-L 1799-4934 **ISSN (printed)** 1799-4934 **ISSN (pdf)** 1799-4942

Location of publisher Espoo **Location of printing** Helsinki **Year** 2013

Pages 145 **urn** http://urn.fi/URN:ISBN:978-952-60-5178-9

Tekijä
Panu Vesanen

Väitöskirjan nimi
Yhdistetty ultramatalan kentän MRI ja MEG: instrumentaatio ja sovelluksia

Julkaisija Perustieteiden korkeakoulu

Yksikkö Lääketieteellisen tekniikan ja laskennallisen tieteen laitos

Sarja Aalto University publication series DOCTORAL DISSERTATIONS 87/2013

Tutkimusala Lääketieteellinen tekniikka ja biofysiikka

Käsikirjoituksen pvm 11.01.2013 **Väitöspäivä** 24.05.2013

Julkaisuluvan myöntämispäivä 10.04.2013 **Kieli** Englanti

☐ **Monografia** ☒ **Yhdistelmäväitöskirja (yhteenveto-osa + erillisartikkelit)**

Tiivistelmä

Magneettikuvaus (MRI) on tekniikka, jolla voidaan noninvasiivisesti kuvantaa aineen sisäistä rakennetta. MRI ei tuota ionisoivaa säteilyä ja saatujen kuvien kontrastia voidaan manipuloida monipuolisesti, minkä vuoksi magneettikuvausta käytetään laajalti apuna lääketieteellisessä tutkimuksessa ja diagnostiikassa. Perinteisesti magneettikuvauksen signaali-kohinasuhde kasvaa käytetyn kentän kasvaessa, mikä on ohjannut MRI-laitteiden kehitystä kohti yhä korkeampia kentän voimakkuuksia.

Ultramatalan kentän (ULF) MRI on uusi tekniikka, jossa mikroteslaluokan magneettikenttiä käytetään kuvan muodostamiseksi. Matalaa signaali-kohinasuhdetta pystytään osittain kompensoimaan prepolarisoimalla näyte 1 – 200 mT kentässä ja käyttämällä suprajohtavia kvantti-interferenssilaitteita (SQUID) signaalin keräykseen. ULF MRI:n etuja ovat joustava ympäristö sekvenssikehitykseen, ainutlaatuiset kontrastimekanismit ja mahdollisuus rakentaa äänetön ja geometrialtaan avoin laite. ULF MRI on myös yhteensopiva magnetoenkefalografian (MEG) kanssa. Tämän ansiosta on mahdollista rakentaa hybridilaite, jolla pystytään kuvantamaan sekä ihmisaivojen rakennetta että toimintaa samanaikaisesti.

Tämä väitöskirja käsittelee kuvatunlaisen MEG-MRI-laitteen suunnittelua, rakentamista ja testaamista. Laite perustuu kaupalliseen koko pään kattavaan MEG-laitteeseen, johon yhdistettiin ULF MRI -toiminnallisuus. Väitöskirjatyössä tutkittiin, miten magneettisesti suojatun huoneen sisällä pulsoivat magneettikentät käyttäytyvät. Pulsoimisesta syntyvien haitallisten pyörrevirtojen kumoamiseksi kehitettiin polarisaatiokela, joka synnyttää vain pienen hajakentän ympärilleen. Lisäksi SQUID-sensoreita kehitettiin kenttäkestoisemmiksi siten, että ne säilyttävät toimintakykynsä myös voimakkaiden polarisaatiopulssien jälkeen. Lopulta laitetta käytettiin mittaamaan MEG-signaalia ja ULF MR -kuvia ihmisen aivoista.

Yllä kuvatun laitteistokehityksen lisäksi väitöskirjassa tutkittiin myös ULF MRI:n sovelluksia. Virrantiheyden kuvantamiseksi kehitettiin menetelmä, jossa käytetään hyväksi ULF MRI:n joustavuutta koodaamalla hyötysignaali ilman ulkoista magneettikenttää. Lisäksi relaksaatioaikojen lämpötilariippuvuutta tutkittiin. Merkittäviä vaihteluja löydettiin riippuen kentän voimakkuudesta. Saatuja tuloksia käytettiin lämpötilakarttojen muodostamiseen.

Tässä väitöskirjassa esitetyt tulokset osoittavat, että kaupalliseen MEG-laitteeseen on mahdollista lisätä MRI-toiminnallisuus. Tämänkaltainen laite mahdollistaa uusien aivotutkimusmenetelmien kehittämisen. Ainutlaatuisen matalakenttäkontrastin hyödyntäminen on mielenkiintoinen aihe tuleville tutkimuksille.

Avainsanat Magneettikuvaus, MRI, ultramatalan kentän MRI, magnetoenkefalografia, MEG, MEG-MRI, SQUID

ISBN (painettu) 978-952-60-5177-2 **ISBN (pdf)** 978-952-60-5178-9

ISSN-L 1799-4934 **ISSN (painettu)** 1799-4934 **ISSN (pdf)** 1799-4942

Julkaisupaikka Espoo **Painopaikka** Helsinki **Vuosi** 2013

Sivumäärä 145 **urn** http://urn.fi/URN:ISBN:978-952-60-5178-9

Preface

I still remember vividly walking into the office of Prof. Risto Ilmoniemi in February 2006. Back then, as a freshman applying for a summer job, I could have never imagined that I would someday be sitting in the very same laboratory preparing for my doctoral defense. The Department of Biomedical Engineering and Computational Science (BECS) has literally been my second home during the eight years of my university studies. During the undergraduate studies, here I would find help to finish my exercises, and during the graduate studies, here I would find support in times that publishing seemed like an endless struggle.

For my stay at BECS, I would like to express my gratitude to Prof. Risto Ilmoniemi above all. Without your supervision and guidance this Thesis would not have been possible. I appreciate the independence you gave me, it served as a great motivator. Dr. Jaakko Nieminen I would like to thank for the seven years we worked together. I value your dedication, thoroughness, and reliability. I am grateful to Koos Zevenhoven for the fruitful discussions we had and all the constructive criticism you gave me. I am impressed by the scope of knowledge you have. Juhani Dabek I would like to thank for the collaboration we had and the good mood that you brought to the lab. Prof. Fa-Hsuan Lin and Yi-Cheng Hsu I would like to thank for the time we worked together both in Finland and abroad, I am inspired by your diligence and ability to adapt to working in a changing environment. I also enjoyed a lot working with Dr. Antti Ahonen, Dr. Juha Simola, Dr. Juha Hassel, Prof. Lauri Parkkonen, Dr. Jari Penttilä, Dr. Roberto Tejera-Garcia, Dr. Jyrki Mäkelä, Prof. Jukka Sarvas, Juho Luomahaara, Sarianna Alanko, Andrey Zhdanov, and Mika Pollari.

This thesis was made financially possible by the European Community's Seventh Framework Programme (FP7/2007–2013) under Grant Agreement No. 200859, Instrumentarium Science Foundation, Emil Aaltonen

Foundation, and International Doctoral Programme in Biomedical Engineering and Medical Physics (iBioMEP). The manuscript of this Thesis was markedly improved by the comments from the preliminary examiners Prof. Alexander Braginski and Dr. Gösta Ehnholm to whom I am very thankful.

All my friends I would like to thank for the great time we have had together. With you, it was easy not to think about science! My girlfriend Hanna I would like to thank for being such a pölö. I am deeply grateful for all the moments of laugh and joy we have experienced together. Finally, I would like to express my gratitude to my parents Marja and Tuomo and brothers Sampo and Kari for the constant support and encouragement throughout my life.

Espoo, May 2, 2013,

Panu Vesanen

Contents

List of Publications

This Thesis consists of an overview and the following Publications, which are referred to in the text by their Roman numerals.

I P. T. Vesanen, J. O. Nieminen, K. C. J. Zevenhoven, J. Dabek, J. Simola, J. Sarvas, and R. J. Ilmoniemi. The spatial and temporal distortion of magnetic fields applied inside a magnetically shielded room. *IEEE Transactions on Magnetics*, 48, 53–61, January 2012.

II J. O. Nieminen, P. T. Vesanen, K. C. J. Zevenhoven, J. Dabek, J. Hassel, J. Luomahaara, J. S. Penttilä, and R. J. Ilmoniemi. Avoiding eddy-current problems in ultra-low-field MRI with self-shielded polarizing coils. *Journal of Magnetic Resonance*, 212, 154–160, September 2011.

III J. Luomahaara, P. T. Vesanen, J. Penttilä, J. O. Nieminen, J. Dabek, J. Simola, M. Kiviranta, L. Grönberg, C. J. Zevenhoven, R. J. Ilmoniemi, and J. Hassel. All-planar SQUIDs and pickup coils for combined MEG and MRI. *Superconductor Science and Technology*, 24, 075020, June 2011.

IV P. T. Vesanen*, J. O. Nieminen*, K. C. J. Zevenhoven, J. Dabek, L. T. Parkkonen, A. V. Zhdanov, J. Luomahaara, J. Hassel, J. Penttilä, J. Simola, A. I. Ahonen, J. P. Mäkelä, and R. J. Ilmoniemi. Hybrid ultra-low-field MRI and magnetoencephalography system based on a commercial whole-head neuromagnetometer. *Magnetic Resonance in Medicine*, in press, 2013.

V P. T. Vesanen, J. O. Nieminen, K. C. J. Zevenhoven, Y.-C. Hsu, and R. J. Ilmoniemi. Current-density imaging using ultra-low-field MRI with zero-field encoding. Submitted to *Magnetic Resonance Imaging*, 2013.

VI P. T. Vesanen, K. C. J. Zevenhoven, J. O. Nieminen, J. Dabek, L. T. Parkkonen, and R. J. Ilmoniemi. Temperature dependence of relaxation times and temperature mapping in ultra-low-field MRI. Submitted to *Journal of Magnetic Resonance*, 2013.

*The first two authors contributed equally to this study.

Author's Contribution

Publication I: "The spatial and temporal distortion of magnetic fields applied inside a magnetically shielded room"

The author formulated the problem, developed the theory, investigated its validity by measurements, and interpreted the results. He is the principal writer of the article.

Publication II: "Avoiding eddy-current problems in ultra-low-field MRI with self-shielded polarizing coils"

The author is a co-inventor of the method[1]. He was responsible for the experimental part of the work including the construction of the coils. He took part in interpreting the results and editing the manuscript for publication.

Publication III: "All-planar SQUIDs and pickup coils for combined MEG and MRI"

The author was responsible for a large part of the measurements and participated in interpreting their results. He took part in editing the manuscript for publication.

[1] J. O. Nieminen, P. T. Vesanen, K. C. J. Zevenhoven, and R. J. Ilmoniemi. System and method for prepolarizing magnetic resonance- or relaxation-based measurements. Patent pending PCT/FI2011/050367, filed April 21, 2011.

Publication IV: "Hybrid ultra-low-field MRI and magnetoencephalography system based on a commercial whole-head neuromagnetometer"

The author performed a large part of the experimental work, analyzed the data, and contributed to interpreting the results. He also took part in nearly all parts of the work related to the construction of the system. He is the main writer of the article together with the second author.

Publication V: "Current-density imaging using ultra-low-field MRI with zero-field encoding"

The author devised the method, performed simulations, and contributed to interpreting their results. He is the main writer of the manuscript.

Publication VI: "Temperature dependence of relaxation times and temperature mapping in ultra-low-field MRI"

The author performed the measurements, reviewed and applied the theory, and interpreted the results. He is the principal writer of the manuscript.

List of Abbreviations

DC	Direct current
MEG	Magnetoencephalography
MRI	Magnetic resonance imaging
MSR	Magnetically shielded room
NMR	Nuclear magnetic resonance
SNR	Signal-to-noise ratio
SQUID	Superconducting quantum interference device
ULF MRI	Ultra-low-field MRI

1. Introduction

Magnetic resonance imaging (MRI) is a noninvasive method that is used to study the interior structure of matter [1]. Due to its capability to produce excellent soft tissue contrast without the use of ionizing radiation, MRI has become a widely spread imaging modality utilized for both medical diagnosis and research. The signal-to-noise ratio (SNR) of an MRI measurement scales with the strength of the magnetic field applied to the imaging volume [2, 3]. This has driven the development of modern MRI scanners towards ever higher tesla-range magnetic fields.

In contrast to the development trend of high-field scanners, MRI measurements in microtesla-range magnetic fields have been demonstrated recently [4, 5]. In this approach, called ultra-low-field (ULF) MRI, the sample is prepolarized [6] in a millitesla-range magnetic field, and superconducting quantum interference devices (SQUIDs) [7] are used for detecting the signal in any chosen microtesla or even nanotesla-range magnetic field. ULF MRI has the potential to complement conventional high-field MRI by enabling measurements in a low-field environment, which possibly offers unique advantages and applications.

The contrast mechanisms provided by ULF MRI are significantly different from those available to high-field scanners. ULF MRI is sensitive to slow kilohertz-range molecular motions, and the field strength can be chosen to probe the tissue with a wide range of frequencies. Furthermore, in contrast to high-field scanners, the low applied fields allow the design of a silent device with relaxed geometry constraints. Finally, the combined use of low fields and SQUIDs for signal detection make ULF MRI compatible with magnetoencephalography (MEG) [8], which uses SQUIDs to measure the magnetic field generated by neuronal activity in the brain. A hybrid scanner involving both MEG and MRI capabilities allows imaging of the structure and function of the brain with a single device [5].

1.1 Aims of the study

The main target of this Thesis (Publications I–IV) was to design, construct, and test a hybrid MEG-MRI device. In the rest of the Thesis, the device will be referred to as the Aalto MEG-MRI prototype. The device was subsequently used to investigate also several other applications of ULF MRI (Publications V and VI). In the following, the aims of the individual publications are listed.

I To understand the spatial and temporal behavior of magnetic fields applied inside a magnetically shielded room (MSR). To learn how to design coils and MSRs suitable for ULF MRI.

II To develop a theoretical framework for designing self-shielded coils for ULF MRI. To construct a self-shielded polarizing coil and experimentally test its shielding properties.

III To investigate whether all-planar thin-film-based SQUID modules can be used for ULF MRI. To develop practical field-tolerant SQUIDs for MEG-MRI.

IV To develop instrumentation for the Aalto MEG-MRI prototype. To use the device for MRI and MEG measurements of the human brain. To validate the quality of the acquired MRI and MEG data with corresponding commercial devices.

V To develop a method for imaging the amplitude and direction of current-density patterns using ULF MRI.

VI To study the temperature dependence of T_1 and T_2 relaxation times at magnetic fields 50 μT – 3 T. To investigate the suitability of ULF MRI for temperature mapping.

2. Theory

In this section, the basic theory of nuclear magnetic resonance (NMR) and MRI will be reviewed. The emphasis is in the aspects relevant for understanding the unique character and advantages of ULF MRI.

2.1 Nuclear magnetism

Nuclear magnetism is a phenomenon whose origin can be explained only in terms of quantum mechanics [2,9,10]. All known elementary particles, such as the nuclei of atoms, have a quantum mechanical property called spin. It is defined by a spin quantum number S, which can only take integer or half-integer values. Spin gives rise to the spin angular momentum operator $\hat{\boldsymbol{S}}$ so that the eigenvalue of $\hat{\boldsymbol{S}}^2$ is $\hbar S(S+1)$, where $h = 2\pi\hbar$ is the Planck constant. The definition of the spin angular momentum is completed by introducing its z component $\hat{\boldsymbol{S}}_z$ with the eigenvalue $\hbar m_S$, where m_S can take any of the $2S+1$ values $-S, -S+1, \ldots, S-1, S$. It can be shown that the nuclear magnetic moment $\boldsymbol{\mu}$ arises from the spin angular momentum, and its strength μ is related to the eigenvalue of $\hat{\boldsymbol{S}}^2$ by

$$\mu = \gamma\hbar\sqrt{S(S+1)}, \tag{2.1}$$

where γ is called the gyromagnetic ratio.

Consider a macroscopic ensemble of N spins with a quantum number S. In the absence of an external magnetic field, the directions of the nuclear magnetic moments μ are random and no macroscopic magnetic moment develops. When nuclei are exposed to an external magnetic field $\boldsymbol{B} = B\boldsymbol{e}_z$, where $\boldsymbol{e}_z$ is the Cartesian unit vector in the z direction, the z component of μ becomes well defined and, when measured, takes one of the values

$$\mu_z = \gamma\hbar m_S. \tag{2.2}$$

To calculate the strength of the developing macroscopic magnetic moment,

the energy E of the nuclear magnetic moment in the external magnetic field is needed,

$$E = \boldsymbol{\mu} \cdot \boldsymbol{B} = \mu_z B = \gamma \hbar m_S B. \tag{2.3}$$

The proportion of spins n_{m_S} with a quantum number m_S is given by the Boltzmann distribution: the z component of the macroscopic magnetic moment in thermal equilibrium, m_z^0, is given by

$$m_z^0 = \sum_{j=1}^{N} \mu_z = N\gamma\hbar \sum_{m_S} n_{m_S} \tag{2.4}$$

$$= N\gamma\hbar \frac{\sum_{j=-S}^{j=S} j \exp\left(\gamma\hbar j B / k_\mathrm{B}\theta\right)}{\sum_{j=-S}^{j=S} \exp\left(\gamma\hbar j B / k_\mathrm{B}\theta\right)} \tag{2.5}$$

$$\approx N\gamma\hbar \frac{\sum_{j=-S}^{j=S} j(1 + \gamma\hbar j B / k_\mathrm{B}\theta)}{\sum_{j=-S}^{j=S} (1 + \gamma\hbar j B / k_\mathrm{B}\theta)} \tag{2.6}$$

$$= \frac{N\gamma^2\hbar^2 S(S+1)}{3k_\mathrm{B}\theta} B, \tag{2.7}$$

where θ is the temperature, and k_B is the Boltzmann constant. The approximation in Eq. (2.6) was $\gamma\hbar B / k_\mathrm{B}\theta \ll 1$, which holds very well in room temperature and for magnetic field strengths that can be generated in practice. It can be seen from Eqs. (2.7) and (2.1) that nuclear magnetism develops only for nuclei with $S \neq 0$. Since the discovery of effective methods to measure the phenomenon [11, 12], nuclear magnetism has been a subject of intensive research with a number of wide-spread applications.

2.2 The Bloch equation

In the previous section, the origin of the macroscopic magnetic moment was outlined. However, the strength of the magnetic moment is so weak that its measurement is difficult in a static setup. According to classical electromagnetism [13], a magnetic moment $\boldsymbol{m}$ experiences in an external magnetic field $\boldsymbol{B}$ a torque $\boldsymbol{T}$ equal to

$$\boldsymbol{T} = \boldsymbol{m} \times \boldsymbol{B}. \tag{2.8}$$

On the other hand, Newton's second law applied to torque reads

$$\boldsymbol{T} = \boldsymbol{r} \times \boldsymbol{F} = \boldsymbol{r} \times \frac{d\boldsymbol{p}}{dt} = \frac{d\boldsymbol{J}}{dt}, \tag{2.9}$$

where $\boldsymbol{r}$ is a vector of location, $\boldsymbol{F}$ force, $\boldsymbol{p}$ the classical momentum, and $\boldsymbol{J}$ the classical angular momentum, which is related to the magnetic moment by $\boldsymbol{m} = \gamma \boldsymbol{J}$ in close analogy with its quantum mechanical version in

Eq. (2.1). Combining Eqs. (2.8) and (2.9) gives the Bloch equation

$$\frac{d\boldsymbol{m}}{dt} = \gamma \boldsymbol{m} \times \boldsymbol{B}, \tag{2.10}$$

which can also be written in matrix form

$$\frac{d\boldsymbol{m}}{dt} = \mathbf{A}\boldsymbol{m} \ , \tag{2.11}$$

where

$$\mathbf{A} = \gamma \begin{pmatrix} 0 & B_z & -B_y \\ -B_z & 0 & B_x \\ B_y & -B_x & 0 \end{pmatrix} . \tag{2.12}$$

If the magnetic moment at $t = 0$ is $\boldsymbol{m}_0$ and $\boldsymbol{B}$ is constant in time, the solution of this equation is

$$\boldsymbol{m} = e^{\mathbf{A}t}\boldsymbol{m}_0 = \mathbf{R}\boldsymbol{m}_0, \tag{2.13}$$

where $\mathbf{R} = e^{\mathbf{A}t}$ is an orthogonal rotation matrix. Equation (2.13) describes the precession of the magnetic moment $\boldsymbol{m}$ about the magnetic field $\boldsymbol{B}$. The angular frequency of the precession is called the Larmor frequency

$$\omega_{\mathrm{L}} = \|\mathbf{A}\|_2 = \gamma|\boldsymbol{B}|, \tag{2.14}$$

where $\|\mathbf{A}\|_2$ denotes the spectral norm of $\mathbf{A}$.

The precession of the magnetic moment in a constant field $\boldsymbol{B} = \boldsymbol{B}_0$ can be manipulated by applying a magnetic field $\boldsymbol{B}_1(t)$ that rotates in the plane perpendicular to $\boldsymbol{B}_0$ in resonance with the magnetic moment, *i.e.,* at the Larmor frequency. To understand the mechanism of the phenomenon, consider a frame of reference that rotates at the Larmor frequency. In this frame, the magnetic moment appears to be static when $\boldsymbol{B}_1 = 0$. As soon as $\boldsymbol{B}_1$, which also appears static in the rotating frame, is turned on, the magnetic moment starts precessing around $\boldsymbol{B}_1$ in the rotating frame. In this way, short $\boldsymbol{B}_1$ pulses can be used to flip the direction of the magnetic moment, *e.g.,* to induce precession of the magnetic moment. The axis and angle of the flip are determined by the phase and amplitude of the pulse, respectively. A noteworthy property of this resonance phenomenon is that the relative strengths of $\boldsymbol{B}_0$ and $\boldsymbol{B}_1$ do not play a role. As long as $\boldsymbol{B}_1$ is rotating at the Larmor frequency, spin flips can be made regardless of whether the amplitude of $\boldsymbol{B}_1$ is tiny, equal, or large compared to B_0.[1]

[1] Spin flips can be achieved also with an $\boldsymbol{B}_1$ field oscillating in a single direction. In this case, ideal spin flips require $B_1 \ll B_0$.

2.3 The imaging equation

Nuclear magnetism can be used for imaging by realizing what can be done if the strength of the external field $\boldsymbol{B}$ is made spatially varying. According to Eq. (2.14), the precession frequency of the magnetic moment will in this case also depend on the location. The magnetic field of the total magnetic moment distribution can subsequently be measured by any magnetic field detector. In this section, quantitative expressions for encoding spatial information into the NMR signal will be developed without making any assumptions about the strengths or shapes of the magnetic fields nor on the type of the magnetic field detector.

Specifically, consider a magnetic field $\boldsymbol{B}_\mathrm{s}$ generated by a unit current in the pick-up coil of any magnetic field sensor. According to the principle of reciprocity, the magnetic flux ϕ through the coil due to a magnetic moment distribution $\boldsymbol{m}$ is

$$\phi = \int (\boldsymbol{B}_\mathrm{s} \cdot \boldsymbol{m}) d\boldsymbol{r}. \tag{2.15}$$

By using the solution of the Bloch Equation (2.13), the result can also be written

$$\phi = \int \boldsymbol{B}_\mathrm{s}^\top \mathbf{R} \boldsymbol{m}_0 \, d\boldsymbol{r} = \int \boldsymbol{e}^\top \boldsymbol{m}_0 \, d\boldsymbol{r}, \tag{2.16}$$

where $\boldsymbol{e} = \mathbf{R}^{-1} \boldsymbol{B}_\mathrm{s}$, and $^\top$ denotes the transpose. The imaging problem of MRI can be seen from Eq. (2.16): Find the distribution of magnetic moment $\boldsymbol{m}_0$ by using the signal ϕ of a magnetic field detector. To represent the problem digitally and evaluate the results numerically, spatial discretization of the magnetic moment distribution is often performed.

To discretize Eq. (2.16), it is useful to decompose $\boldsymbol{m}_0$ and $\boldsymbol{e}$ by

$$\begin{cases} \boldsymbol{m}_0 = \sum_{i=1}^N \eta_i \boldsymbol{h}_i + \Delta_{\boldsymbol{m}_0} \\ \boldsymbol{e} = \sum_{i=1}^N \epsilon_i \boldsymbol{h}_i + \Delta_{\boldsymbol{e}} \end{cases}, \tag{2.17}$$

where the vectors $\boldsymbol{h}_i$ belong to any set of linearly independent vectors that spans the three-dimensional vector space; $\Delta_{\boldsymbol{m}_0}$ and $\Delta_{\boldsymbol{e}}$ are residuals that can be made arbitrarily small by using a large enough N. Using these decompositions and approximating $\Delta_{\boldsymbol{m}_0} = \Delta_{\boldsymbol{e}} = 0$, Eq. (2.16) can be rewritten as

$$\phi = \boldsymbol{\epsilon}^\top \mathbf{H} \, \boldsymbol{\eta}, \tag{2.18}$$

where the elements of $\mathbf{H}$ are

$$H_{ij} = \int \boldsymbol{h}_i \cdot \boldsymbol{h}_j \, d\boldsymbol{r}, \tag{2.19}$$

and the elements of the vectors $\boldsymbol{\epsilon}$ and $\boldsymbol{\eta}$ are ϵ_i and η_i, respectively. To solve the vector $\boldsymbol{\eta}$ defining the magnetic moment distribution, also time needs to discretized. Let us define that the basis functions $\boldsymbol{h}_i$ are time-independent and the coefficients ϵ_i are time dependent. Using these, a time-discretized version of Eq. (2.18) can be written as

$$\boldsymbol{\phi} = \mathbf{E}\mathbf{H}\boldsymbol{\eta}, \tag{2.20}$$

where the elements of $\boldsymbol{\phi}$ are $\phi(t_i)$ and the rows of $\mathbf{E}$ are $\boldsymbol{\epsilon}(t_i)^\top$. In this Thesis, Eq. (2.20) is referred to as the imaging equation. If the encoding-matrix $\mathbf{E}\mathbf{H}$ is of full rank, the solution of Eq. (2.20) is

$$\boldsymbol{\eta} = (\mathbf{E}\mathbf{H})^{-1}\boldsymbol{\phi} \tag{2.21}$$

assuming the magnetic moment and the time are discretized in the same number of elements such that the inverse exists. Obviously, also under- and over-determined systems of the imaging equation can be considered. Moreover, the generalization of Eq. (2.20) in the case of a detector array is straightforward.

2.4 Relaxation theory

In the previous sections, the effects of dissipation on the dynamics of the nuclear magnetism were neglected. The energy dissipation of a spin system, *i.e.,* relaxation, can be properly explained only by quantum mechanics [9, 14–17]. However, in the following, I shall outline a semi-classical treatment of the relaxation processes [10, 18], which gives qualitatively correct results in many applications.

Suppose there is a system of identical spins with $S = 1/2$ in an external magnetic field $\boldsymbol{B}_0 = B_0\boldsymbol{e}_z$. In this field, according to Eq. (2.3), an energy gap $\Delta E = \gamma\hbar B_0 = \hbar\omega_\mathrm{L}$ develops between the spins with $m_S = -1/2$ and $m_S = 1/2$. Thus, only energy quanta of frequency ω_L are able to flip spins between the states.

Suppose there is an additional time-dependent field $\boldsymbol{B}(t) = B_x(t)\boldsymbol{e}_x$, where $B_x(t)$ is a random function of time with the average $\langle B_x(t)\rangle = 0$. Furthermore, suppose the auto-correlation function

$$G(\tau, t) = \langle B_x(t)B_x(t+\tau)\rangle \tag{2.22}$$

is stationary, *i.e.,* $G(\tau, t) = G(\tau)$ and time reversible, *i.e.,* $G(-\tau) = G(\tau)$. A random field with these properties could arise, *e.g.,* from thermal motion

of the surrounding nuclei. However, as mentioned previously, only quanta of frequency ω_{L} are able to interfere with the spin population. Therefore, it is useful to inspect the Fourier transform of $G(\tau)$,

$$H(\omega) = \int_{-\infty}^{\infty} G(\tau) e^{-i\omega\tau} d\tau, \tag{2.23}$$

where the imaginary unit i is defined by $i^2 = -1$. A common model for the auto-correlation funtion is $G(\tau) = \langle B_x^2 \rangle e^{-|\tau|/\tau_{\mathrm{c}}}$, where τ_{c} describes the correlation time. The exponential form of the auto-correlation function follows, *e.g.,* from isotropic molecular motion governed by the diffusion equation [9]. With this assumption, the Fourier transform of the auto-correlation function becomes

$$H(\omega) = 2\langle B_x^2 \rangle \frac{\tau_{\mathrm{c}}}{1 + (\omega\tau_{\mathrm{c}})^2}. \tag{2.24}$$

Let us proceed to calculating the dynamics of the z component of the magnetic moment m_z described by populations n_+ and n_- of spins in the $m_S = 1/2$ and $m_S = -1/2$ states. In thermal equilibrium, the number of spins flipping from the $m_S = -1/2$ state to the $m_S = 1/2$ state has to be equal to the number of those flipping in the opposite direction,

$$n_-^0 W_+ = n_+^0 W_-, \tag{2.25}$$

where n_+^0 and n_-^0 are the thermal equilibrium spin populations described by the Boltzmann distribution, W_+ describes the rate of spin flips from the $m_S = -1/2$ to the $m_S = 1/2$ state, and W_- is the opposite rate. The mean transition rate W can be related to Eq. (2.23) by applying the Fermi golden rule[2] [18]

$$W = \frac{W_- + W_+}{2} = \frac{1}{2}\gamma^2 H(\omega). \tag{2.26}$$

The kinetic equations for the populations n_+ and n_- are

$$\begin{cases} \dfrac{dn_+}{dt} = W_+ n_- - W_- n_+ \\ \dfrac{dn_-}{dt} = -W_+ n_- + W_- n_+ \end{cases}. \tag{2.27}$$

By combining Eqs. (2.25)–(2.27) and (2.7), a differential equation

$$\frac{dm_z}{dt} = -2W(m_z - m_z^0), \tag{2.28}$$

can be derived for $m_z = \frac{1}{2}\gamma\hbar(n_+ - n_-)$. If an initial condition $m_z(0) = 0$ is assumed, Eq. (2.28) has a solution

$$m_z(t) = m_z^0(1 - e^{-2Wt}). \tag{2.29}$$

[2]Strictly speaking, Fermi golden rule predicts $W_+ = W_-$. However, the result is modified such that non-zero thermal equilibrium populations can develop. This obscure, but necessary modification is discussed in detail in Ref. [18].

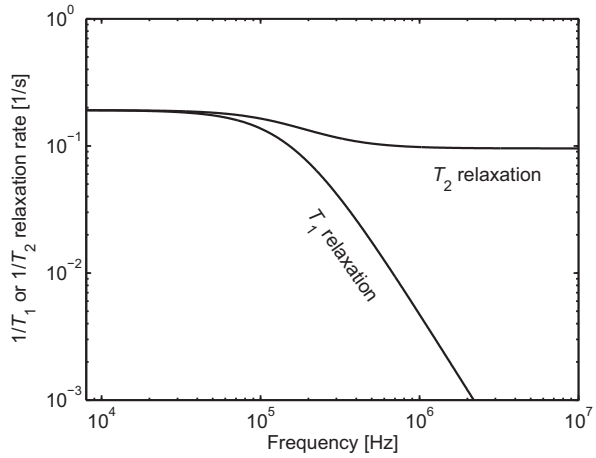

Figure 2.1. The frequency dependence of T_1 and T_2 relaxation times. The parameters used in the plot are $\gamma = 2.67 \cdot 10^8$ rad^{-1}T^{-1}, $\langle B^2 \rangle = (2\ \mu\text{T})^2$, and $\tau_\text{c} = 1$ µs.

The time constant $1/2W$ of the exponential decay in Eq. (2.29) is often written as T_1, which is called the spin–lattice or longitudinal relaxation time. T_1 relaxation time characterizes the time scale with which the spin system returns to thermal equilibrium with its surroundings, *i.e.,* the lattice.

The treatment above can be further generalized by assuming that there is a random field not only in the x direction but also in y and z directions so that $\langle B_x^2 \rangle = \langle B_y^2 \rangle = \langle B_z^2 \rangle$ and $\langle B_x^2 \rangle + \langle B_y^2 \rangle + \langle B_z^2 \rangle = \langle B^2 \rangle$. Using Eqs. (2.24), (2.26), and (2.29), the frequency dependence of T_1 relaxation can be summarized by

$$\frac{1}{T_1} = 2W = \frac{2}{3}\gamma^2 \langle B^2 \rangle \frac{\tau_\text{c}}{1 + (\omega\tau_\text{c})^2}. \tag{2.30}$$

As explained in Section 2.2, the macroscopic magnetic moment can point also transverse to the applied external field. A calculation similar to the one above shows that also the transverse magnetic moment decays exponentially to its equilibrium value zero. The associated time constant is called spin–spin or transverse relaxation time and its frequency dependence can be described as [18]

$$\frac{1}{T_2} = \frac{1}{3}\gamma^2 \langle B^2 \rangle \left(\tau_\text{c} + \frac{\tau_\text{c}}{1 + (\omega\tau_\text{c})^2} \right). \tag{2.31}$$

The frequency dependence of the relaxation times is plotted in Fig. 2.1. It can be seen that both relaxation times increase monotonically with the frequency, or equivalently, the field strength. In the limit $\omega\tau_\text{c} \ll 1$, the relaxation times converge to a plateau, where $T_1 = T_2$. This is natural

as in zero field, one can not distinguish a vector along the field from one perpendicular to it. Finally, the plot shows that changes in T_1 as a function of the frequency can be many decades while the maximum change in T_2 is limited by a factor of two.

Besides varying the field strength, relaxation times can be altered by manipulating τ_c. For example in the case that random rotational motion of molecules is the dominant relaxation process, τ_c is given by [9]

$$\tau_c = \frac{4\pi a^3 \eta}{3k_B\theta}, \tag{2.32}$$

where η is the viscosity and a is the molecular radius. In general, τ_c can be modified by varying the temperature or viscosity.

3. Methods

3.1 High-field MRI

High-field MRI is a wide-spread imaging technology capable of producing millimeter-resolution images of the structure of human body. The medical applications of MRI are diverse: it is used, *e.g.,* in anatomical imaging of the whole body, functional brain imaging [19, 20], diffusion imaging [21, 22], angiography [23, 24], elastometry [25], and thermometry [26]. Since its introduction in the 1970s, MRI has been a subject of intensive research.

High-field MRI is based on a static and homogeneous magnetic field $\boldsymbol{B}_0 = B_0 \boldsymbol{e}_z$ that generates a strong thermal equilibrium magnetization as described in Section 2.1. The tesla-range $\boldsymbol{B}_0$ field is typically generated by a superconducting magnet, which can not be switched off during the measurement. To induce a precession signal, the magnetization can be flipped to the xy plane by a 90° $\boldsymbol{B}_1$ AC pulse at the Larmor frequency. The magnetic field produced by the precessing x and y components of the magnetization can be measured by induction coils tuned to the Larmor frequency. However, the precessing magnetization dephases exponentially because of T_2 relaxation and inhomogeneities in the $\boldsymbol{B}_0$ field. Simultaneously with the precession and dephasing, the z component of the magnetization recovers towards thermal equilibrium because of T_1 relaxation. Thus, an MRI sequence typically consists of several such excitations followed by a period of magnetization manipulation and signal detection.

To acquire images with high-field MRI, the scanner typically includes also three spatially varying gradient fields produced by resistive magnets. The gradient fields are typically designed so that each of them provides a linear gradient along one of the Cartesian axes. When superposed onto

B_0, the linear gradients encode spatial information about the magnetization in the phase of the precessing magnetic moments. With a suitable sequence of gradient field pulsing, the encoding matrix $\mathbf{E}$ in Eq. (2.20) can be arranged to form a Fourier matrix. Furthermore, typically the space is discretized to rectangular voxels, in which case the matrix $\mathbf{H}$ in Eq. (2.20) can be simply written as $\mathbf{H} = V\mathbf{I}$, where V is the volume of the voxel and $\mathbf{I}$ is the identity matrix. With these modifications, the solution of the imaging equation (2.20) can be calculated by Fourier transform.

The thermal equilibrium polarization is proportional to the magnetic field strength, and the strength of the precession signal is proportional to the rate of the field change, *i.e.,* the Larmor frequency. Thus, the total signal strength in a high-field MRI measurement depends on the square of the field. This has driven the development of modern MRI scanners towards high magnetic fields of 7 T and above. While the progress has been extremely successful, tesla-range static magnetic fields are not suitable for all applications and patient groups. Imaging of patients, *e.g.,* with metal implants is generally not possible. The static B_0 field restricts also the range of available sequences. In the following, an alternative approach to MRI methodology will be described.

3.2 Ultra-low-field MRI

In contrast to the development of high-field MRI towards stronger magnetic fields, ULF MRI is an emerging approach, in which images are acquired in microtesla-range fields [4,27–30]. However, as discussed in Section 2.3, the signal strength of any MRI measurement depends on the thermal equilibrium magnetization, which is proportional to the strength of the external field. Thus, the magnetization needs to be polarized separately before the signal measurement in microtesla-range fields [6]. Furthermore, signal detection using an antenna based on Faraday's law (Section 3.1) is replaced by detection utilizing SQUIDs [7], which detect the magnetic flux directly. This way, the signal strength depends only on the polarizing field strength but not on the strength of the microtesla-range imaging field. Finally, the ULF-MRI device is usually located in a magnetically shielded room [31] for reduction of the environmental magnetic field noise. In the following subsections, these important aspects of ULF-MRI instrumentation are reviewed. In the last subsections, the advantages, challenges, and applications of ULF MRI are discussed.

3.2.1 Prepolarization

The concept of prepolarization refers to establishing a strong spin polarization before the precession signal is measured at a low $\boldsymbol{B}_0$ field. The simplest method to build up polarization is the application of a strong magnetic field, *i.e.,* prepolarizing field $\boldsymbol{B}_\mathrm{p}$, which causes an energy gap between the spin states of the sample. During the application of $\boldsymbol{B}_\mathrm{p}$, the populations of the the states develop towards a thermal equilibrium determined by the Boltzmann distribution as explained in Section (2.1). The duration of the prepolarization depends on the desired level of polarization so that $\boldsymbol{B}_\mathrm{p}$ is typically applied for a time comparable to T_1 of the sample.

After a sufficiently long period of prepolarization, $\boldsymbol{B}_\mathrm{p}$ can be ramped down in two different ways. If the ramp down is rapid enough, *i.e.,* nonadiabatic, the magnetization at the end of the ramp points in the direction of $\boldsymbol{B}_\mathrm{p}$ and its components perpendicular to $\boldsymbol{B}_0$ start precession. If the ramp down is slow enough, *i.e.,* adiabatic, the magnetization follows the direction of the total field during the ramp and points in the direction of $\boldsymbol{B}_0$ at the end of the ramp. The latter of these the scenarios occurs if the adiabatic condition [32] is satisfied, *i.e.,*

$$\frac{d\psi}{dt} \ll \gamma|\boldsymbol{B}_\mathrm{tot}(t)|, \tag{3.1}$$

where $\boldsymbol{B}_\mathrm{tot}(t) = \boldsymbol{B}_0 + \boldsymbol{B}_\mathrm{p}(t)$ and ψ is the angle between $\boldsymbol{B}_0$ and $\boldsymbol{B}_\mathrm{tot}$. Conversely, the ramp is nonadiabatic if the condition in Eq. (3.1), with $\ll$ replaced by $\gg$, is satisfied.

The requirements for the direction and homogeneity of $\boldsymbol{B}_\mathrm{p}$ depend on the chosen ramp-down method. If the ramp is designed to be non-adiabatic, the optimal direction of $\boldsymbol{B}_\mathrm{p}$ is perpendicular to $\boldsymbol{B}_0$ so that all of the prepolarized magnetization contributes to the precession signal. Furthermore, a homogeneous $\boldsymbol{B}_\mathrm{p}$ is preferable as all the inhomogeneities in the direction of the polarization will transfer to phase differences between the precessing spins. In contrast, such requirements do not exist if the system is designed to use adiabatic ramp down of $\boldsymbol{B}_\mathrm{p}$. However, in this case an excitation pulse can be used to induce the precession. The coil required for producing excitation pulses slightly complicates the experimental setup and applying the pulse takes away a few milliseconds of the time available for signal acquisition.

The main design criterion for the polarizing coil is to maximize the magnetic field in a region of interest given a fixed level of power. When im-

plemented using resistive materials such as copper, these requirements typically lead to heavy coils. Moreover, all the power fed into the coil will be dissipated as heat so that active cooling of the polarizing coil is often necessary. Finally, the dewar housing the SQUIDs restricts the geometry of the coil so that practically feasible designs often result in excessively large coils. In the Aalto MEG-MRI prototype, these problems were addressed by constructing a superconducting polarizing coil. The required liquid helium is readily available, the coil can be made light, and it can be located close to the region of interest. To mitigate the increase in helium boil-off because of the necessary junction to a resistive material, high-T_c leads[1] were used to transfer the junction close to the neck plug of the dewar.

Alternative methods for prepolarization

In addition to prepolarization by a strong DC magnetic field, there are also several other prepolarization methods. Prepolarization using the Overhauser effect [33] is based on irradiating a sample containing unpaired electrons with a field corresponding to the electron spin resonance. As a result, a part of the electron spin polarization will relax into hydrogen polarization that, under favourable conditions, can increase several orders of magnitude compared to the thermal equilibrium magnetization at the same field strength. Applying the Overhauser effect as a prepolarization method for ULF MRI was presented in Ref. [34]. A significant drawback of this promising method is that it requires material with unpaired electrons, *i.e.,* free radicals. Such materials are naturally scarce in the body so that injecting them as a contrast agent is typically needed.

Another method of prepolarization is optical pumping [35], which enables MRI of noble gases. In optical pumping, circularly polarized light is applied to a spin system, causing the transfer of angular momentum from the photons to the spin system. With such a method, the polarization of nonzero spin noble gases, such as ^{3}He or ^{129}Xe, can reach levels that become useful, *e.g.,* for imaging of lungs. Low-field MRI with optical pumping was demonstrated in Ref. [36]. The combination of optical pumping with ULF MRI is especially promising [37] since the level of the spin polarization is independent of the applied magnetic field. Combined with the fact that the sensitivity of SQUID detection does not depend on the field strength, this implies that the total SNR of the measurement is

[1] High-T_c materials are superconducting already at a temperature of liquid nitrogen.

independent of the applied magnetic field. Therefore, the quality of lung images obtained with optically polarized gases could be equal regardless of whether the signal is acquired at ULF using SQUIDs or at tesla-range fields using conventional methods.

3.2.2 SQUID sensors

SQUID theory

A SQUID sensor [7] is a highly sensitive magnetometer based on Josephson junctions [38] and flux quantization. If a magnetic field is applied through a superconducting loop having two Josephson junctions[2], a shielding current starts circulating the loop so that the the total flux through the loop becomes restricted to an integer number of flux quanta $h/2e$, where h is the Planck constant and e is the elementary charge. By applying a biasing current above the critical current of the junctions, the changes in magnetic flux can be measured from the voltage across the junctions. In practice, the junctions have also resistance and capacitance which complicate the function of the SQUID.

The energy resolution of a SQUID is proportional to the square root of its inductance and capacitance [7]. Therefore, the physical size of a SQUID is usually minimized to maximize its energy sensitivity. In contrast, the magnetic field sensitivity increases with the size of the coil detecting the flux. These two contradicting requirements are met by using a separate superconducting coil, *i.e.,* pick-up coil for detecting the flux. The pick-up coil is in series with a signal coil that is inductively coupled to the SQUID loop. This kind of a structure is called a flux transformer and its function is to focus the detected flux into the SQUID. An optimal size and configuration of the pick-up loop depends on the application. Common configurations are a single loop that detects the magnetic field component normal to the coil, a figure-of-eight coil that detects a transverse gradient of a field component normal to the coil, and an axial gradiometer that measures the longitudinal gradient of the field.

Ideally, a SQUID acts as a flux-to-voltage transducer so that the voltage depends sinusoidally on the flux applied to the pick-up coil. For practical applications, the response is typically linearized by operating the SQUID in a flux-locked-loop mode. In this mode, the flux threading the SQUID

[2]Here, the function of a DC SQUID is explained. Also radio-frequency SQUIDs exist [7].

loop is canceled by an equivalent amount of flux applied from a separate feedback coil. The strength of the feedback flux is determined by monitoring the voltage over the SQUID. In flux-locked-loop mode, the measured signal is actually the current applied to the feedback coil.

Other types of sensors for ULF MRI

A superconductor is characterized by the temperature T_c below which it turns to the superconducting state. The SQUIDs have traditionally been manufactured using low-T_c materials that require immersion in liquid helium to reach the superconducting state. However, SQUIDs made from high-T_c materials are available as well [7]; they are designed to work in temperatures provided by liquid nitrogen. In addition, several other types of highly sensitive magnetometers have been reported: atomic magnetometers [39] are based on optical pumping of alkali atoms whose interaction with the magnetic field can be measured. Mixed sensors [40] are based on a giant-magnetoresistive component coupled to a flux-to-field transformer. In a large part of the published work for ULF MRI, including this Thesis, low-T_c SQUIDs have been used for signal detection. However, low-field MRI has also been demonstrated using a high-T_c SQUID [41,42], an atomic magnetometer [43], and a mixed sensor [44].

SQUIDs in ULF MRI

Using low-T_c SQUIDs for the detection of the ULF-MRI signal poses additional challenges for their design. The millitesla-range prepolarizing fields may cause flux trapping in the superconducting structures of the SQUID. Flux trapping is caused by flux vortices that penetrate type-II superconductors, such as niobium, when the applied magnetic field exceeds the lower critical field B_{c1} of the material. When the magnetic field is removed, the vortices may remain in the material causing a remnant magnetic field. In addition, after the field removal, the vortices may reorganize themselves for a minimum-energy configuration; the reorganization may appear as noise in the SQUID signal. Many of the important aspects of flux trapping are predicted by the Bean model [45].

The problem of flux trapping in the SQUID structures has typically been solved by placing the SQUID inside a superconducting shielding enclosure [27, 30]. The pick-up coil is left outside the enclosure so that the sensitivity to magnetic field is preserved. However, when the pick-up coil is placed in a strong magnetic field, it transforms the flux to the SQUID, causing strong shielding currents that may cause flux trapping. Such a

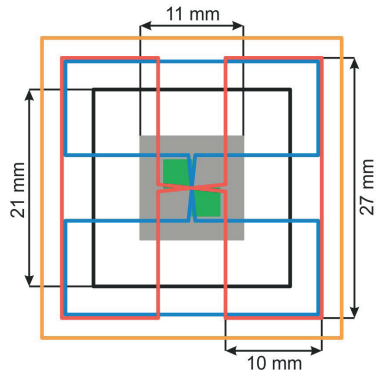

Figure 3.1. The geometry of a SQUID module including its outline (orange), a magnetometer loop (black), two orthogonal planar gradiometers (blue and red), the shielding niobium plate (gray) and two SQUID chips (green).

problem is prevented by limiting the current in the flux transformer by using a flux dam [46], also known as a Q-spoiler. The flux dam consists of a Josephson junction or an array of junctions connected in series with the flux transformer. When the current exceeds the junction's critical current, the junction becomes resistive limiting the current in the flux transformer.

The design of SQUID sensors in the Aalto MEG-MRI prototype (Publication III) is based on the planar modules used in a commercial MEG system [47]. These all-planar modules include both the pick-up coils and the SQUID (Fig. 3.1), they can be manufactured using thin-film technology, and the installation of the modules to the system is based on a plug-in principle. However, the composite design complicates the shielding of the SQUID against the magnetic fields used in ULF MRI. Currently, the solution is to use small niobium plates below and on top of the modules. Another problem is that the thin-film leads of the pick-up loop intrinsically focus field around their edges, which leads to flux trapping in the pick-up coil and noise in the subsequent measurement. Such flux trapping is minimized in the current design by using thin-film strips as narrow as 6 µm. It has been predicted that in such a narrow strip and with B_0 below 60 µT, the total energy of the system is minimized when no flux vortices are present in the material [48].

3.2.3 Magnetically shielded room

A magnetically shielded room (MSR) is, in the context of biomagnetism, a space of several tens of cubic meters surrounded by walls made of materials with high conductivity and permeability [31, 49]. The purpose of

an MSR is to shield its interior against the environmental magnetic field, whose magnitude exceeds the noise level of, *e.g.,* SQUIDs. The walls of an MSR typically consist of multiple layers of two different types. The innermost layer is often made from μ metal, whose relative permeability μ_r can be between 10000 and 100000. The purpose of the high-permeability layer is to guide the low-frequency (< 100 Hz) components of the magnetic field around the interior of the room. The outermost layer of an MSR is typically made from a well-conducting material such as aluminum. Its purpose is to shield against higher frequency magnetic field components (> 100 Hz) by forming eddy current loops that generate a magnetic field opposing the original disturbing field. The shielding performance of the room can be further increased by adding more such pairs of layers; currently the best-shielded room in the world has 8 layers [50].

There are several challenges in operating a ULF-MRI system inside an MSR. First, the millitesta-range polarizing field applied inside the shielded room may magnetize the μ metal walls of the MSR causing an unwanted remnant field that may distort the applied imaging fields. Even stronger magnetic fields will cause saturation of the μ metal, which can degrade the shielding performance of the room. Second, ramping of the polarizing and gradient fields during a ULF-MRI sequence causes changing magnetic fields that induce eddy currents in the conductive layers of the MSR. These eddy currents generate a secondary magnetic field inside the room, disturbing the imaging, *e.g.,* by dephasing the spins or saturating the SQUIDs.

MSRs have typically been built for shielding MEG systems that require suppression of low-frequency environmental magnetic field components down to 1 Hz and even below. If ULF MRI is operated only with Larmor frequencies of several kilohertz or above, the necessary shielding can be achieved with a significantly lighter MSR. There is no need for the μ metal layers, and also the conductive paths in the aluminum layers can be restricted [51]. These modifications largely reduce the harmful effects of the MSRs. Recently, ULF-MRI also completely without an MSR was demonstrated [52]. However, if Larmor frequencies below 1 kHz are needed or if the device is designed to measure MEG together with ULF MRI, heavy shielding is needed and such simplifications to the design of the MSR can not be made.

In this Thesis, a significant effort was made to quantitatively understand the spatial and temporal shape of the secondary magnetic fields

caused by applying and ramping the MRI fields (Publication I). It was found that to mitigate the adverse effects of the secondary magnetic fields, it is crucial that the μ metal layer is the innermost layer of the MSR. Furthermore, it is beneficial to minimize the dipole moments of the MRI coils and to locate the MEG-MRI system in the middle of the MSR. As a result of the theoretical work, a self-shielded polarizing coil, which has a dipole moment close to zero, was implemented in the Aalto MEG-MRI prototype (Publication II). Ramping of such a coil induces only weak eddy currents to the conductive walls of an MSR, enabling ULF MRI also in a heavily shielded room.

3.2.4 ULF-MRI sequences and reconstruction

In a large part of the ULF-MRI-related work published so far, the sequences and reconstruction have been similar to those used in high-field MRI. In the context of the imaging equation (2.20), this implies that the space is discretized in Cartesian voxels so that $\mathbf{H} = V\mathbf{I}$, and the matrix $\mathbf{E}$ simplifies practically to the Fourier transform matrix. In the following, a typical ULF-MRI sequence is described in more detail. Advantages of exploiting the full form of Eq. (2.20) are discussed in Section 3.2.5.

A basic ULF-MRI sequence for one-dimensional imaging is presented in Fig. 3.2. In the simplest case, the $\boldsymbol{B}_0$ field and one of the gradient fields, *i.e.,* the frequency-encoding gradient are kept at a constant value throughout the sequence. The sequence begins with a polarizing-field pulse that magnetizes the sample as described by the exponential development of the x component of the magnetization M_x. The polarizing field is switched off adiabatically so that the magnetization turns along the z axis, *i.e.,* parallel to $\boldsymbol{B}_0$. A $\boldsymbol{B}_1$ pulse is applied to flip the magnetization back to the xy plane, where the magnetization starts precession and dephasing in the $\boldsymbol{B}_0$ and gradient fields. A spin echo [3] is prepared by applying a second $\boldsymbol{B}_1$ pulse. SQUID acquisition is currently not possible during the $\boldsymbol{B}_1$ pulses; the useful MRI signal consists of the echo that occurs after the second $\boldsymbol{B}_1$ pulse.

If the gradient field is spatially linear and its amplitude is small compared to B_0, an image of a sample can be reconstructed by Fourier transforming the acquired signal. By adding pulses with gradient fields that vary also in the other spatial dimensions, two- or three-dimensional images can be acquired by phase encoding [3]. Another option is to acquire many one-dimensional projections with a sequence similar to that

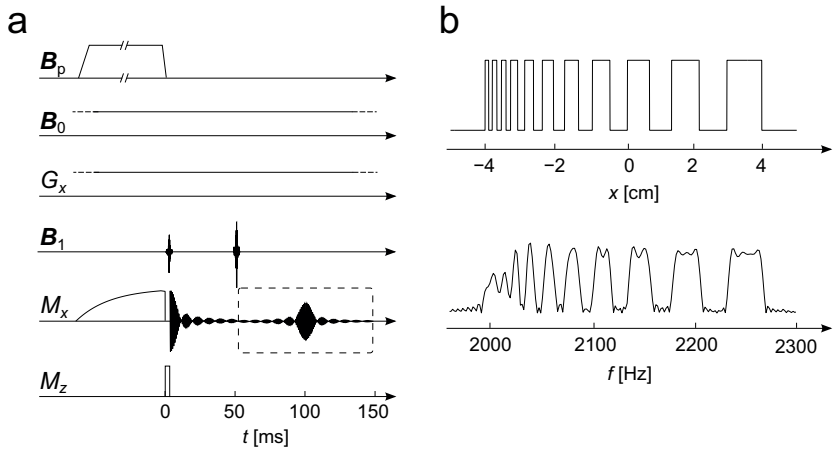

Figure 3.2. In (a), a prepolarized spin-echo sequence and development of the magnetization. The time axis before 0 ms is not drawn to scale; a typical polarizing pulse is longer. The $\boldsymbol{B}_0$ strength is 50 μT, the gradient strength G_x is 100 μT/m, and the echo time is 100 ms. The dashed box indicates the MRI signal that is used to reconstruct the image; the duration of the data acquisition equals the echo time. In (b), the one-dimensional sample to be imaged and its simulated ULF-MRI reconstruction by Fourier transform. It can be seen that with the chosen gradient strength and data acquisition time, the gross features of the sample (its rightmost part) are resolved well while the finest features (the leftmost part) are not.

in Fig. 3.2. The axis of the projection can be changed by applying linear combinations of the available gradients. After reconstructing a suitable amount of one-dimensional projections, an image can be formed using the inverse Radon transform [3] in a way resembling the reconstruction in computed tomography.

It is noteworthy that slice selection [3] in ULF MRI is difficult and impractical for many applications. Selecting, say, a z-directional slice is based on using a pulse of G_z gradient to develop a large bandwidth of precession frequencies in the z direction. During the gradient pulse, a frequency-selective $\boldsymbol{B}_1$ pulse can be applied to flip the spins, whose precession frequency belongs to the frequency band of the $\boldsymbol{B}_1$ pulse. In ULF MRI, however, the bandwidth of precession frequencies over, *e.g.,* a 20-cm region of interest is 850 Hz, when a 100-μT/m gradient is applied. To accurately select a 1-cm thick slice, corresponding to a band of 42 Hz, a $\boldsymbol{B}_1$-pulse length of several times $1/(42\text{ Hz}) = 24$ ms would be required. For most applications, this is an excessively long time, as T_2 relaxation times of tissues are typically on the order of 100 ms. Two-dimensional imaging is still possible, but the resulting image will be a projection, in which structures in the dimension that was not encoded will be presented

on top of each other. A novel possibility to perform slice selection in ULF MRI would be to develop a gradient in the polarizing field and apply the excitation pulse during the polarization.

Compared to high-field MRI, the sequences of ULF MRI are relatively inefficient, because the magnetization recovers only during the prepolarization. For example in Publication IV, over 80% of the total imaging time was spent on polarizing the sample.

Multi-channel detection

The SNR of an MRI measurement can be increased by acquiring the signal with multiple detectors [53]. A multichannel ULF-MRI system can be conveniently built around an existing MEG device (see Section 3.3), which readily provides an array for up to 306 detectors. The optimal multichannel reconstruction method depends mainly on the dominant noise sources, the desired application, and available SNR. In ULF MRI, the reconstruction from N-channel data is typically derived to voxel-wise maximize the SNR of the composite image [53–55]. Specifically, first N single-channel images are reconstructed independently, and subsequently the images are combined voxel-wise by

$$I = \frac{\boldsymbol{s}^* \boldsymbol{\Sigma}^{-1} \boldsymbol{v}}{\boldsymbol{s}^* \boldsymbol{\Sigma}^{-1} \boldsymbol{s}}, \tag{3.2}$$

where I is the composite image voxel value, $\boldsymbol{v}$ is an N-element vector containing the single-channel voxel values, $\boldsymbol{s}$ is an N-element vector containing the sensitivity of each detector in the voxel location, * denotes the complex conjugate, and $\boldsymbol{\Sigma}$ is an $N \times N$ noise covariance matrix of the detector array[3].

There are several options for determining the vector $\boldsymbol{s}$ describing the sensitivity of the detector array. The sensitivities can be calculated if accurate information about the detector array geometry and sample positioning are available [56]. This is a particularly attractive option in the context of ULF MRI, as the sample itself does not have an effect on the shape of the sensitivity profiles, because the Larmor frequency is sufficiently low. An alternative option is to estimate the sensitivities from the acquired images by fitting a slowly varying function to the images. However, the accuracy of the method is compromised, *e.g.,* by contrast variations in the sample. A third method makes use of a separate homogeneous sample to measure the single-channel sensitivities by using the

[3]In Eq. (3.2), complex formulation of the MRI data is assumed: the real and imaginary parts of $\boldsymbol{s}$ and $\boldsymbol{v}$ correspond to the x and y components of the magnetization, respectively.

same sequence that was used for the original image.

The optimal geometry of a ULF-MRI detector array depends at least on the desired application and on the dominant noise sources of the system. For SQUID-based MRI of the brain, the optimal number of the elements and their size, shape, and orientation has been discussed in Refs. [55,57,58]. According to the studies, using sensors larger than those used in MEG [59] may be advantageous for ULF MRI, especially if the measurement noise is sensor-dominated.

3.2.5 Advantages of ULF MRI

There are several advantages in measuring NMR and MRI using SQUIDs and magnetic fields of microtesla range and even below.

Relaxed homogeneity requirements

One of the first advantages proposed for ULF MRI was the observation that when the relative field homogeneity $\Delta B/B$ is held fixed, the absolute spectral resolution Δf scales as the magnetic field B [60], *i.e.,*

$$\Delta f = \gamma \Delta B = \gamma \frac{\Delta B}{B} B. \tag{3.3}$$

Exploiting this, spectrometers operating at micro- and nanotesla fields were constructed [60, 61] using relatively simple instrumentation. The intrinsic spectral resolution of such systems is limited only by the lifetime of the signal, determined by the T_2 relaxation time, and high-resolution NMR spectra can be resolved. Moreover, as the SQUID is a broadband device, it is possible to detect the spectra of multiple nuclei at the same time [60].

It has also been envisioned that the enhancement in the NMR spectral resolution could be transferred into enhancement of the spatial resolution of ULF-MR images. However, in imaging applications, the bandwidth of the signal can be increased to maximize the data rate. Extreme spectral resolution is therefore not required; the resolution needs only to be sufficiently high so that strong enough gradient fields, corresponding to bandwidth, can be generated without instrument problems. In any case, the high intrinsic spectral resolution allows flexibility in the sequence design, when applications with specific requirements arise.

Relaxation dispersion and the connection with $T_{1\rho}$

The frequency dependence of relaxation times, *i.e.,* relaxation dispersion described by Eqs. (2.30) and (2.31), has been studied extensively [62–66]

and its theoretical basis [14] was presented already in the 1940s shortly after the dawn of NMR. In the context of SQUID-detected MRI, the relaxation dispersion was first demonstrated in Ref. [67], where it was shown that, as the field decreases, T_1 of agarose gel decreases steeply at fields around 10 mT and reaches a plateau at fields below 1 mT. Moreover, it was shown that the T_1 contrast between gels with different agarose concentrations was greater at the microtesla fields compared to the tesla-range fields. Unfortunately, in this initial study, T_2 relaxation times of the gel were not measured. In Publication VI, it is shown that in microtesla-range fields, the T_2 relaxation time for agarose gel actually equals the T_1 relaxation time as theoretically predicted. Furthermore, it was found that the agarose gel T_2 contrast measured in a tesla-range field does not significantly differ from the $T_1 = T_2$ contrast at microtesla fields. Similar observations were made for brain white and gray matter in Ref. [68].

Despite the above-mentioned issues concerning improved T_1 contrast for agarose gel, studies of the relaxation dispersion for biological tissue and other materials are useful. The field ranges with steep changes in relaxation times can be used to generate dispersion contrast [69–71]. In general, the whole shape of the available dispersion curve can be used to optimize the contrast [72]. Finally, in addition to possible benefits in image contrast, the shape of the dispersion curve reveals details about molecular dynamics in the sample being studied.

In general, the relaxation properties at low frequencies can also be studied with high-field scanners. The $\boldsymbol{B}_1$ field can be used not only to flip the spins but also to induce precession in the rotating frame. The relaxation times in the rotating frame are called $T_{1\rho}$ and $T_{2\rho}$ and they depend on the $\boldsymbol{B}_1$ strength that determines the precession frequency in the rotating frame. Imaging using $T_{1\rho}$-weighted contrast has been applied, *e.g.,* to delineate cartilage [73], diseased muscle tissue [74], and gliomas [75]. A disadvantage of $T_{1\rho}$ imaging especially at 3 T and above is the energy deposition in the tissue due to the required long radio-frequency pulses [76]. However, it has been argued that $T_{1\rho}$ measured in a high-field scanner is roughly equivalent to T_1 measured in a microtesla-range field, when the $\boldsymbol{B}_0$ of the low-field measurement equals the $\boldsymbol{B}_1$ of the high-field measurement [77]. Thus, it is possible that T_1 studies in ULF MRI could be applied to the medical conditions that high-field $T_{1\rho}$ imaging is currently applied to. One of the advantages of ULF MRI in these studies would be having no danger of excessive energy deposition nor heating of the tissue.

Degrees of freedom in signal encoding

Unlike in high-field MRI, the full form of the imaging equation (2.20) is available for use in ULF MRI. Although using the full form will imply a more complicated reconstruction compared to that by Fourier transform, the increased number of degrees of freedom in the signal encoding can potentially be used to extract information from the imaging target more efficiently. It may be beneficial to abandon the tradition of discretizing the space in rectangular voxels, and try, *e.g.,* tetrahedrons or any application-tailored shape. The spatial and temporal shape of the encoding pulses as well as the geometry of the detector array can be designed to match the desired application. In particular, the low magnetic fields allow flexibility in the sequence design; the ability to switch $\boldsymbol{B}_0$ completely off within the sequence was exploited in Publication V to simulate image acquisition from a current distribution inside a sample.

Unique applications

Several applications of ULF MRI, which are available only in the micro- and nanotesla-range fields, will be listed in Section 3.2.7.

General advantages of low applied fields

Because of the weak applied magnetic fields, ULF MRI has also the following advantages. The device is safer than the high-field instruments: there is no danger of ferromagnetic projectiles nor heating of tissue due to radio-frequency pulses. The device could potentially be safe, *e.g.,* for patients with pace makers. The operation of the device is silent due to the weak Lorentz forces in the coils. Field inhomogeneities caused by susceptibility variations in the sample are less severe and thus the reconstructed images contain less distortions. The geometry of the device can be designed to be open, which allows imaging of claustrophobic patients and facilitates the work of the personnel assisting in the imaging. Finally, consisting of relatively simple instrumentation, a ULF-MRI system could be lighter and cheaper to build than conventional high-field MRI systems.

3.2.6 Challenges of ULF MRI

Signal-to-noise ratio

Improving SNR is the most important challenge in the development of ULF MRI. Currently, the best ULF-MR images of human brain have a modest resolution of $3 \times 3 \times 6$ mm^3 and the acquisition takes 90 min-

utes [5]. There are two principal ways to increase the SNR of a ULF-MRI measurement: increasing the strength of the polarizing field and reducing the noise level of the SQUID sensors.

Increasing the strength of the polarizing field is technically challenging. High currents applied through the polarizing coil typically produce heat to the extent that active cooling is required for continuous operation. A large number of turns in the coil results in high inductance so that high voltages are needed to drive the coil. Both large currents and high voltages place challenging requirements for the electronics driving the coil [78]. Furthermore, switching of a polarizing coil with a large dipole moment induces strong eddy-current transients in the walls of the MSR; with a large polarizing coil, also the effects of the higher-order multipole components may be harmful.

In the Aalto MEG-MRI prototype, some of these problems were circumvented by the introduction of a superconducting polarizing coil (Section 3.2.1). However, a switched superconducting coil has a problem of its own. Flux trapping in the superconducting coil during the polarization causes a remnant magnetic field, which may remain in the imaging volume even after the current in the coil is zero. The strength of the remnant magnetic field scales with the applied polarizing field; a strong enough remnant field, which in our system occurs with polarizing pulses of 23 mT and above, disturbs significantly the following MRI encoding.

Concomitant gradients

The conventional MRI reconstruction by Fourier transform requires that all the magnetic field gradients are linear and all the spins precess around the same axis, *i.e.,* the total magnetic field points everywhere in the same, say, z direction. However, if any gradients exist in the magnetic field, then according to the Maxwell's equations, the field cannot point everywhere in the same direction. The spurious magnetic field components, in x and y direction in this case, are called concomitant gradients. In high-field MRI with a tesla-range $\boldsymbol{B}_0$ field, the concomitant gradients are typically so small that they can be neglected. However, in ULF MRI, where the strengths of the gradient fields and that of $\boldsymbol{B}_0$ are of the same order, the reconstruction by Fourier transform is compromised [79]. This problem can be solved by correcting the k-space phase before applying the Fourier-transform [79], correcting the phase of the signal in post-processing [80] or by devising a general reconstruction that models also the effects of the

concomitant gradients [81].

Verification of the safety

In general, ULF MRI is considered a safer technology than high-field MRI because of the weaker magnetic fields employed. However, prepolarization is a feature which does not exist in conventional scanners; safety issues related especially to the switching of the strong magnetic field[4] should be carefully investigated.

For human subjects, switching of a magnetic field induces an electric field in the tissue. The electric field may stimulate peripheral nerves, or in the worst case, the cardiac or respiratory muscles. The current FDA (U.S. Food and Drug Administration) guideline [82] designed for high-field scanners states that the magnetic field time derivative (dB/dt) should not exceed 20 T/s during a ramp, or as an alternative, volunteer studies can be conducted to determine the dB/dt threshold of peripheral nerve stimulation for each device. One of the reasons for this rather relaxed guideline is that for ramp durations of several hundred microseconds typical in high-field MRI, cardiac muscle stimulation occurs at dB/dt levels of several orders of magnitude higher than that for peripheral nerve stimulation [83]. Thus, peripheral nerve stimulation can be used as a safe indicator for a high level of dB/dt.

In ULF MRI, switching, *e.g.,* a 200-mT polarizing field linearly in 5 ms yields a dB/dt of 40 T/s. For a ramp duration as long as 5 ms, it has been estimated that cardiac stimulation occurs for the most sensitive population percentile already at a level of 80 T/s [83]. Moreover, peripheral nerve stimulation is estimated to occur almost at the same level. Thus, in contrast to high-field MRI, sensations of peripheral nerve stimulation during a ULF-MRI measurement may already indicate dangerously high levels of dB/dt. Naturally, for a ULF-MRI system designed to image, *e.g.,* the head or the extremities, the polarizing field in the heart and lungs is significantly reduced from its maximum. Thus, it is likely that ULF MRI is a safe technology, but it is still useful to revise the dB/dt thresholds of stimulation for peripheral, cardiac, and respiratory muscles for millisecond-range ramp durations.

[4]In high-field MRI, there is rapid field switching as well. However, the maximum amplitude of the switchable gradient fields is only some tens of millitesla, whereas in ULF MRI, polarizing fields of $100 - 200$ mT are desirable.

Competition with field-cycled MRI

In field-cycled MRI and NMR [77, 84], the main homogeneous field is not static but can be switched. In this way, it is possible to polarize the sample in a strong field around 100 mT, reduce the field, *e.g.,* to establish contrast at an arbitrarily low field, and ramp up the field again to measure the signal in a high field using induction coils. In principle, many of the applications requiring extremely low magnetic fields (Section 3.2.7) are available also for the field-cycled systems. To match the sensitivity of SQUID detection, the acquisition field is required to be approximately 100 mT; at this frequency range, it is straightforward to implement instrumentation for induction coils so that the noise of the measurement is limited by the body noise of the subject in the scanner [85, 86]. However, most of the field-cycled systems have, so far, been restricted to NMR [77, 84]. MRI-dedicated systems require a strong magnetic field in a larger volume, which increases the power requirements of the system. It remains to be seen if field-cycled MRI can provide a SQUID- and thereby cryogen-free alternative for imaging at ULF.

3.2.7 Applications of ULF MRI

As both MEG and ULF MRI are measured using SQUID sensors, it is useful to consider their combination in a single device [5, 87, 88]. The results of an MEG study are typically visualized on top of an MR image, which has to be acquired separately. Thus, combination of MEG and MRI in a single device would significantly improve the workflow of MEG studies. Moreover, the co-registration of the MEG and MRI coordinate systems is currently problematic for several reasons. First, the manual registration procedure is vulnerable to errors. Second, the subject is often sitting during an MEG study, whereas in an MRI study, the subject is in a supine position. Thus, the position and also the shape of the brain are different during these two sessions. When both MEG and MRI are acquired during the same session with a single device, the co-registration problem is significantly simplified. In this Thesis, a considerable effort was made to design, construct, and test a hybrid MEG-MRI system. The results of the work are reported in Publication IV.

The ability to directly image the neurophysiology of the brain with MRI (direct neuronal imaging, DNI) has been a long-standing dream of neuroscientists [89]. The brain activity is restricted to frequencies below 1 kHz, which gives ULF MRI a unique mechanism to detect the activity. When

the Larmor frequency ω_{L} of a ULF-MRI system is chosen below 1 kHz, neuronal currents at ω_{L} generate tiny magnetic fields and act as resonant pulses to the spin system [90–93]. Neuronal activity could then be detected as a difference between images acquired with ω_{L} well below 1 kHz and ω_{L} safely above 1 kHz. However, the flip angles of these neuronal resonant pulses are so small that the changes they cause have so far not been reliably detected.

The sensitivity of ULF MRI for cancer detection has been evaluated [94,95]. The presented approaches are based on the differences of T_1 relaxation times between cancerous and healthy tissue. However, in neither of the publications were the results compared to those obtained in high-field scanners. Thus, it seems that ULF MRI is capable of detecting cancerous tissue but it is not yet known how the sensitivity or cost-efficiency compares to that obtained with high-field scanners. Other suggested applications of ULF MRI and NMR are, so far, security surveillance for liquid explosives [96] and uranium [97], quantitative imaging [56], and evaluation of fruit quality [98]. In this Thesis, the range of studied applications were extended by investigating ULF-MRI-based current-density imaging (Publication V) and thermometry (Publication VI).

3.3 Magnetoencephalography

With magnetoencephalography (MEG), one measures the magnetic fields generated by synchronous neuronal activity in the brain [8]. Although the very first MEG measurements were conducted using a single induction coil [99], modern MEG devices use helmet-shaped arrays of up to 306 SQUIDs[5] for magnetic field detection. The amplitudes of the neuronal signals are only hundreds of femtotesla; an MEG device has thus to be operated inside an MSR for suppression of environmental magnetic noise. One of the advantages of MEG in comparison to other brain imaging technologies is its temporal resolution of up to several kilohertz. Clinically approved applications of MEG are, so far, presurgical evaluation of epilepsy and brain tumor patients [102]. In addition, current research subjects of MEG include, *e.g.,* dynamics and topology of networks related to spontaneous brain activity [103], and studies of cognition including attention [104], memory [105], and language [106].

[5] MEG recordings using high-T_{c} SQUIDs [100] and atomic magnetometers [101] have also been demonstrated.

Most of the applications of MEG require localizing the neuronal sources of the magnetic field. This can be done by solving the inverse problem of MEG: find the current distribution in the brain that generates the magnetic field measurements recorded by a SQUID array around the head. Unfortunately, such a problem is ill-posed in the sense that no unique solution exists. However, solutions satisfying a particular constraint can be found. Sometimes it is reasonable to assume that there are only a few local and distinct neuronal sources that can be described as current dipoles; their locations and orientations can be determined by solving a nonlinear minimization problem [107]. Another approach is to limit the locations of the neuronal sources to a finite number so that a linear equation can be constructed relating the strengths of the sources and the measured magnetic field. Such an equation is often under-determined, but a unique solution can be found, *e.g.,* by using the minimum-norm estimate [108, 109], in which the solution with the weakest source strengths is selected to represent the real current distribution.

Another physiologically plausible possibility for source reconstruction is to constrain the locations of the sources to the cortical mantle and assume that their orientations are perpendicular to the cortex [110]. In this way, the dimension of the source space can be reduced, and more accurate current-distribution estimates can be found. However, such anatomy-based methods require the acquisition of an MR image and the reliability of the results depends on the accuracy of the co-registration between the MRI and MEG coordinate systems. By improving the co-registration accuracy, a hybrid MEG-MRI device, as discussed in Section 3.2.7 and Publication IV, could thus improve the source reconstruction performance of an MEG system. A highly accurate co-registration may also enable even more sophisticated constraints to the inverse problem.

4. Summary of Publications

The publications in this Thesis can be divided into two categories. Publications I–IV are related to ULF-MRI instrumentation while Publications V–VI (and partly IV) explore the applications of ULF MRI. In the following, the contents of the publications are summarized.

4.1 Publication I: The spatial and temporal distortion of magnetic fields applied inside a magnetically shielded room

A ULF-MRI system includes several coils situated typically inside an MSR. When, *e.g.,* the polarizing field is ramped down, eddy currents are induced in the conductive walls of the MSR. The eddy currents generate a secondary, decaying magnetic field, an MSR response, that may significantly disturb the ULF-MRI measurement by dephasing the spins and saturating the SQUID sensors. The problem is even more severe in the case of a hybrid MEG-MRI system as heavy shielding is needed, and the time constants of the MSR response decay lengthen.

In Publication I, temporal and spatial properties of the MSR response were studied by modeling and by experiments. By assuming a spherical MSR with a single layer of μ metal and aluminum, analytical expressions for the MSR response could be derived in terms of the multipole representation of the MRI coils. An important result is that the MSR response in this model consists of exponentially decaying modes that have their own time constants and fixed time-independent spatial patterns. Furthermore, a single mode is excited only by a single multipole component of the exciting coil. For example, the dipole component of a coil induces a spatially homogeneous MSR response, and a quadrupolar component induces a response, whose components are spatially linear, crossing zero at the center of the room. In particular, it follows from the model that

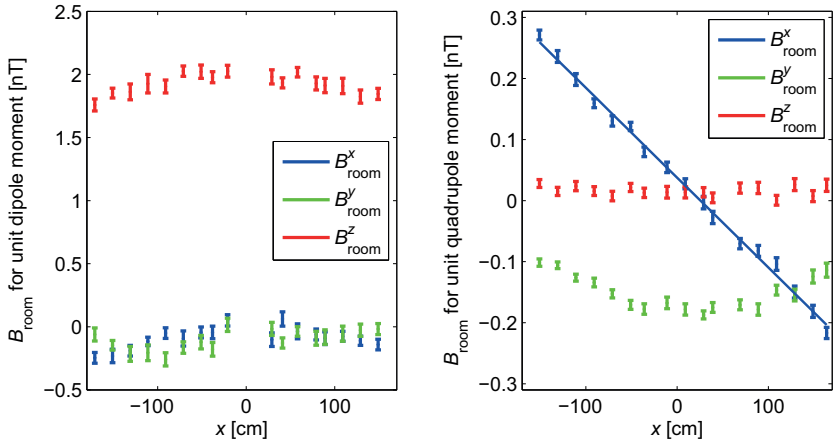

Figure 4.1. Left: the spatial behavior of the MSR response induced by a dipolar polarizing coil (dipole moment z-directional). Right: the spatial behavior of the MSR response induced by a gradient coil that is well described by the multipole component with $l = 2$ and $m = 0$. The solid line is a linear fit to the data.

the dipole component of a coil is the only multipole component that contributes to a nonzero MSR response at the center of the room. An important application of these results is that the MSR response of a dipolar coil can be canceled by constructing a shielding coil with an equal dipole moment in an opposite direction. The dipole moments of the coils can be matched by varying the area and turns of the coils. Thus, it is straightforward to construct a coil pair, which has a zero dipole moment, and still generates a significant field at its center. This kind of a self-shielded coil that induces only a small MSR response near the center of the room was investigated in Publication II.

The applicability of the theoretical predictions were tested experimentally in a rectangular shielded room. It was found out that the decay of the MSR response can be described with a single exponential approximately 100 ms after the polarizing field switch-off. Moreover, Fig. 4.1 shows experimental results about the spatial behavior of the MSR response. It can be seen that the MSR response induced by a dipolar source is fairly uniform near the center of the room. Similarly, the MSR response of a quadrupolar source appears to vary linearly near the center of the room. The largest deviations from the predictions occur near the walls of the room, where the spherical model is a poor approximation of the rectangular MSR.

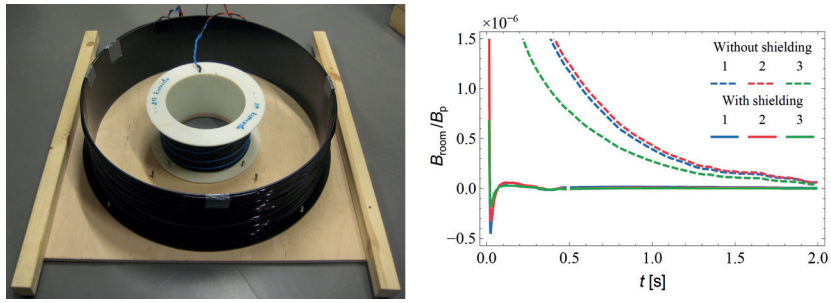

Figure 4.2. Left: A photograph of the constructed polarizing coil surrounded by the shielding coil. Right: Experimental data of the MSR response in three SQUID channels measured with (solid lines) and without (dashed lines) a shielding coil. The polarizing field was ramped down at $t = 0$.

4.2 Publication II: Avoiding eddy-current problems in ultra-low-field MRI with self-shielded polarizing coils

To prevent the harmful effects of the eddy-current-related magnetic fields studied in Publication I, the concept of a self-shielded polarizing coil was investigated in Publication II. By utilizing the multipole expansion, a formalism was developed for designing a shielding coil for any unshielded axially symmetric polarizing coil. Using the formalism, the performance of several shielding geometries was studied. In particular, a simple shielding coil was designed and constructed to null the dipole and quadrupole moments of an existing cylindrical polarizing coil. Fig. 4.2 shows a photograph of the polarizing coil together with the shielding coil, and experimental results demonstrating the shielding efficiency.

4.3 Publication III: All-planar SQUIDs and pickup coils for combined MEG and MRI

In the context of MEG, SQUIDs are designed to operate in a DC magnetic field below some hundreds of nanotesla; the maximum change in the field during an MEG measurement is typically below a few nanotesla. On the other hand, in the context of ULF MRI, the SQUIDs need to tolerate fields of tens of millitesla, recover their full magnetic field sensitivity only tens of milliseconds after the end of the polarizing pulse, and operate in a DC magnetic field of tens of microtesla. In Publication III, the development of the SQUIDs towards these goals is reported.

A field-tolerant MEG-MRI SQUID was developed based on the planar design presented in Fig. 3.1, where the SQUID chip is located on top of

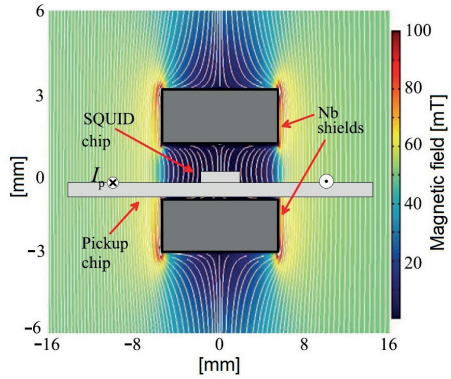

Figure 4.3. Magnetic field around a SQUID module, when a 50-mT homogeneous polarizing field is applied perpendicular to the module. In the superconducting state, niobium can be considered a zero permeability material. Thus, the SQUID chip between the plates is shielded, while the total flux through the pick-up coils remains approximately unchanged.

the planar chip holding the pick-up coils. Shielding of the SQUID was realized by placing niobium plates below and on top of the sensor module. The size of the plates was chosen so that the polarizing field is redirected past the SQUID but the sensitivity to MRI signal is retained as the total flux through the pick-up coil is not significantly altered (Fig. 4.3). The experimental results in Publication III show that by using this design, SQUIDs spontaneously recover after polarizing pulses up to 50 mT.

Unfortunately, the shielding solution described above gives rise to other problems. First, it was found that if the shielding plates are too thin (< 2 mm), polarizing pulses cause flux to trap in the plates leading to inhomogeneities in the $\boldsymbol{B}_0$ field. The problem could be avoided by using plates of at least 2 mm in thickness, in which case no trapped flux could be detected after a polarizing pulses up to 50 mT. Another problem, found after the publication of the article, is that the niobium plates not only redirect the polarizing field, but also distort $\boldsymbol{B}_0$. This problem could be avoided by placing the SQUID modules parallel to $\boldsymbol{B}_0$; in this orientation, the effects of the distortion became insignificant.

As the T_2 relaxation times of tissues are typically around 100 ms, it is important that the SQUIDs recover their full performance as soon after the end of the polarization as possible. However, the experimental results in Publication III show that during the first 100 ms after an 8-mT polarizing pulse, the sensors may exhibit $1/f$ noise that increases the baseline noise level at kilohertz frequencies up to ten-fold. It was hypothesized that the noise originates from the flux that is trapped in the thin-film

pick-up loops during the polarization; the noise would be caused by the rearrangement of the flux vortices after the polarizing field switch-off. Indeed, the contribution of the $1/f$ noise could be removed from the kilohertz range by fabricating thin-film pick-up coils with a narrow linewidth of 6 µm. However, later experiments have shown that if large polarizing fields (> 25 mT) are used, the $1/f$ noise becomes again a dominating noise source in the kilohertz range, even in the case of 3-µm linewidths.

4.4 Publication IV: Hybrid ultra-low-field MRI and magnetoencephalography system based on a commercial whole-head neuromagnetometer

In Publication IV, the development of a hybrid MEG-MRI device is described, and experimental ULF-MRI and MEG results are reported. Photographs of the device and a schematic drawing of the coil system is shown in Fig. 4.4. The hybrid system was developed using parts of an existing MEG device by Elekta Oy which included a liquid helium dewar and

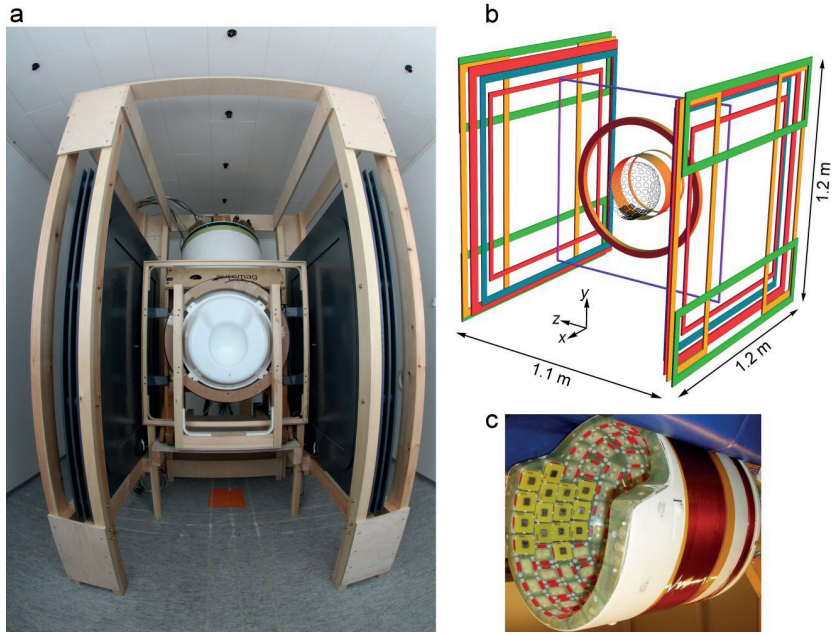

Figure 4.4. In (a), a photograph of the Aalto MEG-MRI prototype without the patient bed. In (b), a schematic representation of the ULF-MRI coil system with the $\boldsymbol{B}_0$ coil (red), three orthogonal gradient coils (yellow, green, and blue), the $\boldsymbol{B}_1$ coil (purple), and the self-shielded polarizing coil (orange). In (c), a photograph of the superconducting polarizing coil wound around the frame holding the SQUID modules.

a helmet-shaped sensor array frame. The frame was equipped with 16 SQUID modules that were installed in the region of the helmet closest to the visual cortex of a subject. In addition, a superconducting polarizing coil was wound around the frame. Its dipole and quadrupole moments were nulled by constructing a superconducting shielding coil, and another resistive shielding coil outside the dewar. Coils for signal encoding were designed and wound in planar PVC plates situated beside the dewar at a distance of 1.1 m from each other.

In the simplest MRI sequences, only $\boldsymbol{B}_0$ and the frequency-encoding gradient are applied during the data acquisition phase. The magnetic field noise originating from the current in these coils was minimized by using batteries as voltage sources; the current in the $\boldsymbol{B}_0$ coil was regulated in addition with a home-made amplifier. The phase-encoding gradients were driven with commercial amplifiers, and the $\boldsymbol{B}_1$ coil was driven with a home-made amplifier; these were situated outside the shielded room. To reduce noise during the data acquisition, these amplifiers were disconnected by mechanical relays during the data acquisition. The software controlling the amplifiers and generating the MRI sequences was written in house. Existing MEG hardware and software could be used for controlling the SQUIDs and acquiring the data.

ULF-MRI results obtained using the device are shown in Fig. 4.5 and MEG results are shown in Publication IV. Several anatomical features can be discerned from the ULF-MRI results and it is shown in Publication IV that the quality of the MEG results is comparable to those obtained with a commercial MEG device. However, it is evident that substantial development is still needed for acquiring ULF-MR images with clinical relevance. In addition, the improvement in the co-registration accuracy remains yet to be demonstrated.

4.5 Publication V: Current-density imaging using ultra-low-field MRI with zero-field encoding

MRI allows the measurement of electric current density; the current-density-associated magnetic field $\boldsymbol{B}_\mathrm{J}$ produces changes to the phase of the precessing magnetization. In high-field MRI, the $\boldsymbol{B}_0$ field is typically orders of magnitude stronger than $\boldsymbol{B}_\mathrm{J}$ so that only the component of $\boldsymbol{B}_\mathrm{J}$ along $\boldsymbol{B}_0$ has a non-negligible effect on the magnetization dynamics. Thus, to acquire information from all three components of the magnetiza-

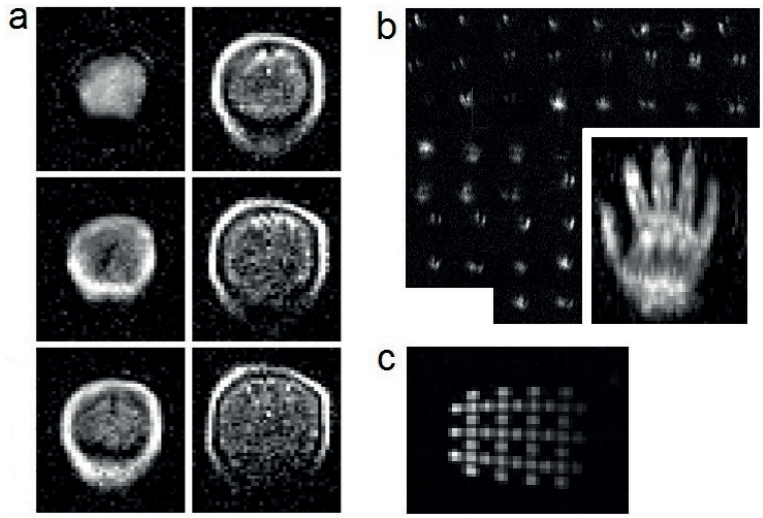

Figure 4.5. Examples of ULF-MR images measured with the Aalto MEG-MRI prototype. In (a), ULF-MR images of human visual cortex published in Publication IV. The resolution is $4 \times 4 \times 6$ mm^3 and the imaging time of the set was 90 minutes. In (b), ULF-MR image of a human hand [111]. The smaller excerpts represent 42 single-channel images and the larger image represents their combination by Eq. (3.2). The resolution is 4×4 mm^2 and the imaging time was 40 minutes. In (c), an ULF-MR image of a rectangular multi-well phantom representing distortion that the concomitant gradients and the remnant field of the polarizing coil can cause, if polarizing field above 23 mT is used. The nominal resolution is 2.6×2.8 mm^2 and the imaging time was 90 minutes. For more discussion about the remnant field of the polarizing coil, see Section 5.

tion, the sample has to be physically rotated twice.

On the other hand, ULF MRI allows easy switching of the microtesla-range $\boldsymbol{B}_0$ field. In Publication V, it is shown that it is possible to acquire information about $\boldsymbol{B}_\mathrm{J}$ by first preparing the magnetization in $\boldsymbol{B}_\mathrm{J}$ without any additional MRI fields, and then recording the signal in $\boldsymbol{B}_0$ in a conventional manner. With this method, all three components of $\boldsymbol{B}_\mathrm{J}$ can be reconstructed without the need to rotate the sample. After acquiring $\boldsymbol{B}_\mathrm{J}$, the current density can be computed simply from Ampere's law. Computational simulations are performed in Publication V to verify the functionality and stability of the method.

4.6 Publication VI: Temperature dependence of relaxation times and temperature mapping in ultra-low-field MRI

T_1 relaxation times at ultra-low fields at a fixed temperature can be drastically different from those at high fields [67,112]. In Publication VI, these

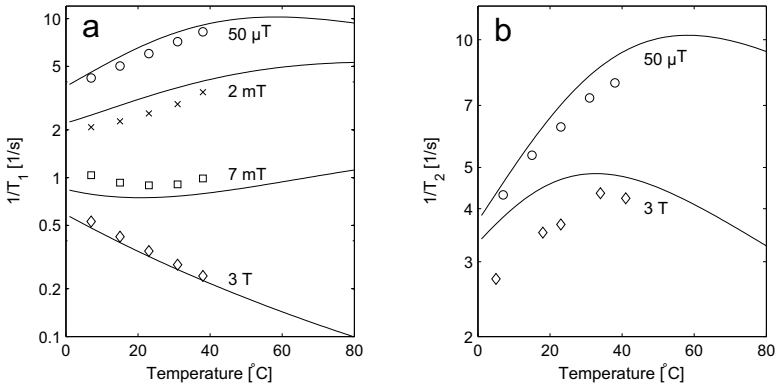

Figure 4.6. The relaxation time T_1 (a) and T_2 (b) measurements overlaid with a model (solid line) derived by assuming that water in agarose gel is present in two different phases with their own relaxation times [113].

results were supplemented by measuring the temperature dependence of T_1 and T_2 relaxation times in agarose gel at different field strengths. Furthermore, two-dimensional temperature maps were measured with ULF MRI by utilizing this temperature dependence.

Fig. 4.6 summarizes the results of the relaxation time measurements reported in Publication VI. In general, it can be seen that both the $1/T_1$ and $1/T_2$ relaxation rates increase as the field strength is decreased. Furthermore, the data verify that, within experimental accuracy, T_1 equals T_2 for agarose gel at microtesla-range fields, as predicted by Eqs. (2.30) and (2.31). Interestingly, it can also be seen that at tesla-range fields, $1/T_1$ decreases as temperature increases while at low fields below a few milliteslas, $1/T_1$ increases as temperature increases. Moreover, at medium fields around 10 mT, $1/T_1$ shows a minimum as a function of temperature. The behavior of $1/T_2$ is somewhat simpler: at a tesla-range field, $1/T_2$ increases as temperature is increased reaching a maximum at around 40 °C. At microtesla range, the maximum of $1/T_2$ seems to be out of the temperature range of the measurements.

The determined quantitative information about the temperature dependence of the relaxation times was utilized by measuring temperature maps of an agarose gel phantom. The results shown in Publication VI demonstrate two-dimensional temperature mapping using ULF-MRI, yielding a spatial resolution of 5×5 mm^2, temporal resolution of 13 minutes, and temperature sensitivity of a few degrees. For practical applications of the method, these figures need to be decreased significantly.

5. Discussion

The first NMR recordings with SQUIDs were conducted in the 1980s and 1990s [114]. The technique was initially used for condensed matter research, where the sample was immersed in the liquid helium together with the SQUID. However, the potential of SQUID detection for MRI was not realized until 2004, when researchers at the University of California, Berkeley, USA demonstrated SQUID-detected MRI of a room temperature sample [4]. In their initial demonstration, they used a single SQUID coupled to a second-order axial gradiometer to image a bell pepper that was polarized in a field of 300 mT produced by a resistive magnet. Later, they showed also in vivo images of human wrist polarized in a field of 30 mT [28].

Combined MRI and MEG measurements were first presented by researchers at the Los Alamos National Laboratories, USA [5, 87]. In their approach, MRI and MEG signals are detected using an array of seven SQUIDs coupled to second-order axial gradiometers, and spins are polarized by a resistive magnet providing fields up to 30 mT. In their initial demonstration [5], they provided ULF-MR images of human brain with $3 \times 3 \times 6$ mm^3 resolution; the imaging time was 90 minutes. To demonstrate the MEG capability of the device, they recorded auditory evoked potentials from the same subject directly after the ULF-MRI scan.

In this Thesis, several novel concepts for the instrumentation of hybrid MEG-MRI were introduced. While the existing devices are based on custom-made SQUIDs and dewars, the Aalto MEG-MRI prototype is based on a commercial whole-head MEG system by Elekta Oy, Finland. Furthermore, this prototype features SQUIDs coupled to magnetometers and first-order planar gradiometers as opposed to the second-order axial gradiometers in the existing systems. Finally, the Aalto MEG-MRI prototype includes for the first time a superconducting coil for ULF-MRI

polarization. These differences in the design give rise both to several advantages and challenges for the Aalto system.

The larger number of sensors, the helmet-shaped dewar, and the MEG-optimized configuration of the array [59] arguably make the MEG capability of the Aalto MEG-MRI protype superior to the existing systems. The sensors based on thin-film technology can also be manufactured in large quantities easily, facilitating the possible commercialization of MEG-MRI. However, the above-mentioned design differences lead also to several technical challenges as discussed in this Thesis. The magnetometers and the first-order gradiometers are significantly more vulnerable to changes in the external magnetic field, such as the MSR response discussed in Publication I, than the second-order gradiometers. The choice of incorporating the SQUID and the pick-up coils in the same module also creates difficulties in the shielding of the SQUID as discussed in Publication III. It may be possible to address these problems by a more careful choice of materials used in the sensors and their shielding. Another possibility is to separate the pick-up coil from the SQUID chip, as has been done in the existing ULF-MRI systems.

As discussed in 3.2.1, the superconducting coil in the Aalto MEG-MRI system enables a compact, light, and efficient method for spin prepolarization. In contrast to the resistive polarizing coils, it also requires no additional cooling besides the liquid helium readily available for the SQUIDs. However, the remanent magnetic field of the coil (Section 3.2.6) remains a severe problem. Several options for addressing the issue have been suggested. A promising, but technically challenging idea is to quickly degauss the coil before each period of MRI data acquisition. The degaussing waveform could be included in the ramp-down of the polarizing field. However, implementation of such a method places challenging requirements for the amplifier driving the coil. Another idea is to correct the inhomogeneity of B_0 caused by the remanent field by shimming with additional coils wound around or inside the dewar. Finally, in cases the distortion caused by the remanent field is not too severe, it may also be possible to correct the distortions in the images by modifying the image reconstruction accordingly [81]. It may, however, be excessively difficult to satisfactorily solve these problems related to the remanent field. In this case, the superconducting polarizing coil could be replaced with a large actively-cooled resistive coil.

In the microtesla field range and below, the T_1 relaxation times of vari-

ous liquid materials can be drastically different from those at tesla-range fields (Fig. 2.1). Therefore, it is possible that in a low field, contrast between, *e.g.,* some types of tissues could be enhanced. However, at least the basic theories of relaxation predict that, in sufficiently low fields, $T_1 = T_2$, and that T_2 changes only moderately as a function of the field strength. The latter has been confirmed also experimentally for many tissues [62, 68]. Thus, when proposing that T_1 contrast between specific materials is enhanced in low fields, it is important to compare the result not to T_1 contrast in high fields but to the corresponding T_2 contrast. Furthermore, it might be possible that the largest contrast enhancements are obtained at around fields in which the rate of T_1 change, dT_1/dB, is the largest. At these fields, the T_1 contrast could be sufficiently different from both the T_1 and T_2 contrast at a high-field, and also the T_1 dispersion contrast can be utilized [70]. Another interesting option is to study possibilities of taking advantage of the quadrupole dips [84] in the T_1 dispersion curves of tissues with heavy protein content.

In Publication IV, combined MEG and MRI measurements were demonstrated using the Aalto MEG-MRI prototype. However, so far, MEG and MRI were measured in separate sessions. An interleaved measurement would be significantly more time-efficient. MEG stimuli are typically delivered at intervals of a few seconds; the idle time between the stimuli could be used for ULF-MRI polarization. After polarization, it is, in principle, possible to acquire the ULF-MRI and MEG signals simultaneously, as the frequency bands of the modalities are separated. However, the frequency range of the MSR response (Publication I), induced by the ramping of the polarizing coil, does overlap with that of the MEG signals. Our self-shielded polarizing coil (Publication IV) decreases the amplitude of the MSR response to a level where it does not interfere with the spin dynamics and prevents the saturation of the sensors, but its amplitude is still significant compared to the level of MEG signals [88]. One possibility for eliminating the remaining MSR response is to use the signal-space projection method [115]. As demonstrated in Publication I, a major part of the MSR response consists of magnetic field modes with low spatial frequencies. These modes define a certain low-dimensional subspace in the signal space of an MEG-MRI array. As the MEG signals consist typically of modes with significantly higher spatial frequencies, the low frequency modes of the MSR response could be removed from the signal space by a projection without significantly distorting the original MEG signals.

As described in Section 3.2.5, ULF-MRI devices have several general advantages related to the low applied magnetic fields, such as safety, silence, susceptibility tolerance, and relatively simple and potentially low-cost instrumentation. However, other prepolarization-based systems that use induction coils for detection [86, 116, 117] share the same advantages. The instrumentation of these SQUID-free methods is even simpler and thus also more affordable than the instrumentation for ULF MRI. Therefore, it is important that the development of ULF MRI is concentrated on its unique advantages, such as the relaxation dispersion at microtesla and nanotesla fields or the combined MEG-MRI discussed in this Thesis. Hints for possible new applications can be looked from $T_{1\rho}$ studies conducted at high fields; it is possible that the same phenomena can be measured directly with ULF MRI. Another interesting topic of development is conductivity imaging at frequencies below one kilohertz (related to Publication V); accurate conductivity information of the human brain even at a modest resolution could dramatically improve the accuracy of MEG, electroencephalography [118], and transcranial magnetic stimulation [119].

In addition to its promise in medical applications, ULF MRI may find use also in fundamental physics and chemistry research. For example, by means of ULF NMR, unidentified reactions occurring at a rate below 100 Hz were found in pure water [112], which is considered a very thoroughly studied substance. Moreover, it has been demonstrated that, in low fields, J-coupling spectra [10] can be measured in the absence of the chemical shift [60]. This can prove useful, *e.g.,* in the detection covalent bonds between atoms. In this Thesis, ULF NMR was investigated in Publication VI, where a model was developed to explain the temperature dependence of relaxation times in agarose gel. By ULF NMR, it could be verified that the model, originally developed for megahertz frequencies, holds reasonably well also at kilohertz frequencies. In addition, the experimental results revealed an interesting cross-over phenomenon at the mid-range frequencies.

6. Conclusion

In this Thesis, a hybrid MEG-MRI scanner based on a commercial whole-head MEG device was designed, constructed, and tested. The results presented in Publication IV show that the scanner is capable of producing ULF-MR images with a $4 \times 4 \times 6$ mm^3 resolution in an imaging time of 90 minutes. The quality of the recorded MEG data is roughly comparable to that measured with a commercial device. These results show that upgrading a commercial MEG device with MRI functionality is a feasible concept. Specifically, it was demonstrated that combined MEG and MRI measurements can be conducted with SQUIDs coupled to thin-film based magnetometer and planar gradiometer pick-up coils.

In addition to the development of instrumentation for MEG-MRI, also other applications of ULF MRI were investigated in this Thesis. A method for measuring current densities inside an object was developed in Publication V. Such a measurements can be used, *e.g.,* for noninvasively determining the conductivity of a material. Moreover, the temperature dependence of T_1 and T_2 relaxation times at 50 μT – 3 T was studied in Publication VI. It was found that the temperature dependence itself depends strongly on the field strength. These results were used to form 2D temperature maps of a phantom using ULF MRI at 50 μT.

When devising novel applications for ULF MRI, it is important to consider ULF MRI and high-field MRI not as competing technologies but as methods that complement each other. Due to the intrinsically low SNR, the resolution of ULF-MR images in many applications is not likely to ever match that of the high-field images. Therefore, the development of ULF MRI should be concentrated on the applications that the high-field scanners can not address. These include, *e.g.,* field-cycling methods, studies requiring sensitivity to slow molecular motions, or sensitive hybrid measurements such as MEG-MRI investigated in this Thesis.

Bibliography

[1] P.C. Lauterbur. Image formation by induced local interactions: Examples employing nuclear magnetic resonance. *Nature*, 242:190–191, 1973.

[2] Z.-P. Liang and P.C. Lauterbur. *Principles of Magnetic Resonance Imaging*. IEEE Press Series in Biomedical Engineering. IEEE Press, New York, USA, 2000.

[3] E.M. Haacke, R.W. Brown, M.R. Thompson, and R. Venkatesan. *Magnetic Resonance Imaging: Physical Principles and Sequence Design*. John Wiley, New York, USA, 1999.

[4] R. McDermott, S.K. Lee, B. ten Haken, A.H. Trabesinger, A. Pines, and J. Clarke. Microtesla MRI with a superconducting quantum interference device. *Proc. Natl. Acad. Sci. USA*, 101:7857–7861, 2004.

[5] V.S. Zotev, A.N. Matlashov, P.L. Volegov, I.M. Savukov, M.A. Espy, J.C. Mosher, J.J. Gomez, and R.H. Kraus Jr. Microtesla MRI of the human brain combined with MEG. *J. Magn. Reson.*, 194:115–120, 2008.

[6] M. Packard and R. Varian. Free nuclear induction in Earth's magnetic field. *Phys. Rev.*, 93:941, 1954.

[7] J. Clarke and A.I. Braginski. *The SQUID Handbook*. Wiley-VCH, Weinheim, Germany, 2004.

[8] M. Hämäläinen, R. Hari, R.J. Ilmoniemi, J. Knuutila, and O.V. Lounasmaa. Magnetoencephalography–theory, instrumentation, and applications to noninvasive studies of the working human brain. *Rev. Mod. Phys.*, 65:413–497, 1993.

[9] A. Abragam. *Principles of Nuclear Magnetism*. Oxford University Press, Oxford, United Kingdom, 1961.

[10] M.H. Levitt. *Spin Dynamics*. John Wiley & Sons, Chichester, United Kingdom, 2001.

[11] F. Bloch, W.W. Hansen, and M. Packard. The nuclear induction experiment. *Phys. Rev.*, 70:474–485, 1946.

[12] E.M. Purcell, H.C. Torrey, and R.V. Pound. Resonance absorption by nuclear magnetic moments in a solid. *Phys. Rev.*, 69:37–38, 1946.

[13] J.D. Jackson. *Classical Electrodynamics*. John Wiley & Sons, New York, 3rd edition, 1999.

[14] N. Bloembergen, E.M. Purcell, and R.V. Pound. Relaxation effects in nuclear magnetic resonance absorption. *Phys. Rev.*, 73:679–712, 1948.

[15] A.G. Redfield. On the theory of relaxation processes. *IBM J. Res. Dev.*, 1:19–31, 1957.

[16] R.K. Wangsness and F. Bloch. The dynamical theory of nuclear induction. *Phys. Rev.*, 89:728–739, 1953.

[17] F. Bloch. Dynamical theory of nuclear induction. II. *Phys. Rev.*, 102:104–135, 1956.

[18] C.P. Slichter. *Principles of Magnetic Resonance*. Harper & Row, New York, USA, 1963.

[19] S. Ogawa, T.-M. Lee, A.S. Nayak, and P. Glynn. Oxygenation-sensitive contrast in magnetic resonance image of rodent brain at high magnetic fields. *Magn. Reson. Med.*, 14:68–78, 1990.

[20] J.W. Belliveau, B.R. Rosen, H.L. Kantor, R.R. Rzedzian, D.N. Kennedy, R.C. McKinstry, J.M. Vevea, M.S. Cohen, I.L. Pykett, and T.J. Brady. Functional cerebral imaging by susceptibility-contrast NMR. *Magn. Reson. Med.*, 14:538–546, 1990.

[21] K.-D. Merboldt, W. Hanicke, and J. Frahm. Self-diffusion NMR imaging using stimulated echoes. *J. Magn. Reson.*, 64:479–486, 1985.

[22] D.G. Taylor and M.C. Bushell. The spatial mapping of translational diffusion coefficients by the NMR imaging technique. *Phys. Med. Biol.*, 30:345–349, 1985.

[23] C.L. Dumoulin, S.P. Souza, M.F. Walkerand, and W. Wagle. Three-dimensional phase contrast angiography. *Magn. Reson. Med*, 9:139–149, 1989.

[24] D.G. Nishimura. Time-of-flight MR angiography. *Magn. Reson. Med*, 14:194–201, 1990.

[25] R. Muthupillai, D.J. Lomas, P.J. Rossman, J.F. Greenleaf, A. Manduca, and R.L. Ehman. Magnetic resonance elastography by direct visualization of propagating acoustic strain waves. *Science*, 269:1854–1857, 1995.

[26] V. Rieke and K. Butts Pauly. MR thermometry. *J. Magn. Reson. Imaging*, 27:376–390, 2008.

[27] J. Clarke, M. Hatridge, and M. Mößle. SQUID-detected magnetic resonance imaging in microtesla fields. *Annu. Rev. Biomed. Eng.*, 9:389–413, 2007.

[28] M. Mößle, W.R. Myers, S.-K. Lee, N. Kelso, M. Hatridge, A. Pines, and J. Clarke. SQUID-detected in vivo MRI at microtesla magnetic fields. *IEEE Trans. Appl. Supercond.*, 15:757–760, 2005.

[29] A.N. Matlachov, P.L. Volegov, M.A. Espy, J.S. George, and R.H. Kraus Jr. SQUID detected NMR in microtesla magnetic fields. *J. Magn. Reson.*, 170:1–7, 2004.

[30] V.S. Zotev, A.N. Matlashov, P.L. Volegov, A.V. Urbaitis, M.A. Espy, and R.H. Kraus Jr. SQUID-based instrumentation for ultralow-field MRI. *Supercond. Sci. Technol.*, 20:S367–S373, 2007.

[31] A.J. Mager. Magnetic shields. *IEEE Trans. Magn.*, 6:67–75, 1970.

[32] M. Bernstein, K.F. King, and X.J. Zhou. *Handbook of MRI Pulse Sequences*. Elsevier Academic Press, San Diego, 2004.

[33] A.W. Overhauser. Polarization of nuclei in metals. *Phys. Rev.*, 92:411–415, 1953.

[34] V.S. Zotev, T. Owens, A.N. Matlashov, I.M. Savukov, J.J. Gomez, and M.A. Espy. Microtesla MRI with dynamic nuclear polarization. *J. Magn. Reson.*, 207:78–88, 2010.

[35] W. Happer. Optical pumping. *Rev. Mod. Phys.*, 44:169–249, 1972.

[36] C.H. Tseng, G.P. Wong, V.R. Pomeroy, R.W. Mair, D.P. Hinton, D. Hoffmann, R.E. Stoner, F.W. Hersman, D.G. Cory, and R.L. Walsworth. Low-field MRI of laser polarized noble gas. *Phys. Rev. Lett.*, 81:3785–3788, 1998.

[37] A. Wong-Foy, S. Saxena, A.J. Moulé, H.-M.L. Bitter, J.A. Seeley, R. McDermott, J. Clarke, and A. Pines. Laser-polarized ^{129}Xe NMR and MRI at ultralow magnetic fields. *J. Magn. Reson.*, 157:235–241, 2002.

[38] B.D. Josephson. Possible new effects in superconductive tunneling. *Phys. Lett.*, 1:251–253, 1962.

[39] I.K. Kominis, T.W. Kornack, J.C. Allred, and M.V. Romalis. A subfemtotesla multichannel atomic magnetometer. *Nature*, 422:596–599, 2003.

[40] M. Pannetier, C. Fermon, G. Le Goff, J. Simola, and E. Kerr. Femtotesla magnetic field measurement with magnetoresistive sensors. *Science*, 304:1648–1650, 2004.

[41] R.E. de Souza, K. Schlenga, A. Wong-Foy, R. McDermott, A. Pines, and J. Clarke. NMR and MRI obtained with high transition temperature DC SQUIDs. *J. Braz. Chem. Soc.*, 10:307–312, 1999.

[42] K. Schlenga, R. McDermott, J. Clarke, R.E. de Souza, A. Wong-Foy, and A. Pines. Low-field magnetic resonance imaging with a high-T_c dc superconducting quantum interference device. *Appl. Phys. Lett.*, 75:3695–3697, 1999.

[43] I.M. Savukov, V.S. Zotev, P.L. Volegov, M.A. Espy, A.N. Matlashov, J.J. Gomez, and R.H. Kraus Jr. MRI with an atomic magnetometer suitable for practical imaging applications. *J. Magn. Reson.*, 199:188–191, 2009.

[44] N. Sergeeva-Chollet, H. Dyvorne, J. Dabek, Q. Herreros, H. Polovy, G. Le Goff, G. Cannies, M. Pannetier-Lecoeur, and C. Fermon. Low-field MRI with magnetoresistive mixed sensors. *J. Phys. Conf. Ser.*, 303:012055, 2011.

[45] C.P. Bean. Magnetization of hard superconductors. *Phys. Rev. Lett.*, 8:250–253, 1962.

[46] R.H. Koch, J.Z. Sun, V. Foglietta, and W.J. Gallagher. Flux dam, a method to reduce extra low frequency noise when a superconducting magnetometer is exposed to a magnetic field. *Appl. Phys. Lett.*, 67:709–711, 1995.

[47] A.I. Ahonen, M.S. Hämäläinen, M.J. Kajola, J.E.T. Knuutila, P.P. Laine, O.V. Lounasmaa, L.T. Parkkonen, J.T. Simola, and C.D. Tesche. 122-channel SQUID instrument for investigating the magnetic signals from the human brain. *Phys. Scr.*, T49:198–205, 1993.

[48] G. Stan, S.B. Field, and J.M. Martinis. Critical field for complete vortex expulsion from narrow superconducting strips. *Phys. Rev. Lett.*, 92:097003, 2004.

[49] D. Cohen. Large-volume conventional magnetic shields. *Rev. Phys. Appl.*, 5:53–58, 1970.

[50] J. Bork, H.F. Hahlbohm, R. Klein, and A. Schnabel. The 8-layered magnetically shielded room of the PTB: Desing and construction. *In Proc. 12th Int. Conf. Biomagnetism, Biomag*, pages 970–973, 2000.

[51] K. Zevenhoven. Solving transient problems in ultra-low-field MRI. Master's thesis, Aalto University, Finland. 2011.

[52] H. Dong, L. Qiu, W. Shi, B. Chang, Y. Qiu, L. Xu, C. Liu, Y. Zhang, H.-J. Krause, A. Offenhäusser, and X. Xie. Ultra-low field magnetic resonance imaging detection with gradient tensor compensation in urban unshielded environment. *Appl. Phys. Lett.*, 102:102602, 2013.

[53] P.B. Roemer, W.A. Edelstein, C.E. Hayes, S.P. Souza, and O.M. Mueller. The NMR phased array. *Magn. Reson. Med.*, 16:192–225, 1990.

[54] V.S. Zotev, P.L. Volegov, A.N. Matlashov, M.A. Espy, J.C. Mosher, and R.H. Kraus Jr. Parallel MRI at microtesla fields. *J. Magn. Reson.*, 192:197–208, 2008.

[55] K. Zevenhoven. Performance of sensor arrays for SQUID-detected MRI of the brain. Special assignment, Aalto University, Finland. 2009.

[56] J. Dabek, P.T. Vesanen, K.C.J. Zevenhoven, J.O. Nieminen, R. Sepponen, and R.J. Ilmoniemi. SQUID-sensor-based ultra-low-field MRI calibration with phantom images: Towards quantitative imaging. *J. Magn. Reson.*, 224:22–31, 2012.

[57] K. Zevenhoven and R.J. Ilmoniemi. Performance of SQUID arrays for MRI of the brain. *In Proc. Intl. Soc. Magn. Reson. Med.*, page 4226, 2011.

[58] A.N. Matlashov, E. Burmistrov, P.E. Magnelind, L. Schultz, A.V. Urbaitis, P.L. Volegov, J. Yoder, and M.A. Espy. SQUID-based systems for co-registration of ultra-low field nuclear magnetic resonance images and magnetoencephalography. *Physica C*, 482:19–26, 2012.

[59] A.I. Ahonen, M.S. Hamalainen, R.J. Ilmoniemi, M.J. Kajola, J.E.T. Knuutila, J.T. Simola, and V.A. Vilkman. Sampling theory for neuromagnetic detector arrays. *IEEE Trans. Biomed. Eng.*, 40:859–869, 1993.

[60] R. McDermott, A.H. Trabesinger, M. Mück, E.L. Hahn, A. Pines, and J. Clarke. Liquid-state NMR and scalar couplings in microtesla magnetic fields. *Science*, 295:2247–2249, 2002.

[61] M. Burghoff, S. Hartwig, L. Trahms, and J. Bernarding. Nuclear magnetic resonance in the nanoTesla range. *Appl. Phys. Lett.*, 87:054103, 2005.

[62] P.A. Bottomley, T.H. Foster, R.E. Argersinger, and L.M. Pfeifer. A review of normal tissue hydrogen NMR relaxation times and relaxation mechanisms from 1-100 MHz: dependence on tissue type, NMR frequency, temperature, species, excision, and age. *Med. Phys.*, 11:425–448, 1984.

[63] H.W. Fischer, P.A. Rinck, Y. van Haverbeke, and R.N. Muller. Nuclear relaxation of human brain gray and white matter: Analysis of field dependence and implications for MRI. *Magn. Reson. Med.*, 16:317–334, 1990.

[64] P.A. Rinck, H.W. Fischer, L. Vander Elst, Y. van Haverbeke, and R.N. Muller. Field-cycling relaxometry: medical applications. *Radiology*, 168:843–849, 1988.

[65] V. Graf, F. Noack, and G.J. Béné. Proton spin T_1 relaxation dispersion in liquid H_2O by slow proton-exchange. *J. Chem. Phys.*, 72:861–863, 1980.

[66] J.M. Escanye, D. Canet, and J. Robert. Frequency dependence of water proton longitudinal nuclear magnetic relaxation times in mouse tissues at 20 °C. *Biochim. Biophys. Acta Mol. Cell Res.*, 721:305–311, 1982.

[67] S.K. Lee, M. Mößle, W. Myers, N. Kelso, A.H. Trabesinger, A. Pines, and J. Clarke. SQUID-detected MRI at 132 μT with T_1-weighted contrast established at 10 μT−300 mT. *Magn. Reson. Med.*, 53:9–14, 2005.

[68] V.S. Zotev, A.N. Matlashov, I.M. Savukov, T. Owens, P.L. Volegov, J.J. Gomez, and M.A. Espy. SQUID-based microtesla MRI for in vivo relaxometry of the human brain. *IEEE Trans. Appl. Supercond.*, 19:823–826, 2009.

[69] J.W. Carlson, D.M. Goldhaber, A. Brito, and L. Kaufman. MR relaxometry imaging. Work in progress. *Radiology*, 184:635–639, 1992.

[70] S.E. Ungersma, N.I. Matter, J.W. Hardy, R.D. Venook, A. Macovski, S.M. Conolly, and G.C. Scott. Magnetic resonance imaging with T_1 dispersion contrast. *Magn. Reson. Med.*, 55:1362–1371, 2006.

[71] J.K. Alford, B.K. Rutt, T.J. Scholl, W.B. Handler, and B.A. Chronik. Delta relaxation enhanced MR: Improved activation-specificity of molecular probes through R_1 dispersion imaging. *Magn. Reson. Med.*, 61:796–802, 2009.

[72] J. Nieminen. Ultra-low-field MRI: techniques and instrumentation for hybrid MEG-MRI. Dissertation, Aalto University, Finland. 2012.

[73] A. Borthakur, E. Mellon, S. Niyogi, W. Witschey, J.B. Kneeland, and R. Reddy. Sodium and $T_{1\rho}$ MRI for molecular and diagnostic imaging of articular cartilage. *NMR Biomed.*, 19:781–821, 2006.

[74] A.E. Lamminen, J.I. Tanttu, R.E. Sepponen, H. Pihko, and O.A. Korhola. $T_{1\rho}$ dispersion imaging of diseased muscle tissue. *Brit. J. Radiol.*, 66:783–787, 1993.

[75] H.J. Aronen, U. Abo Ramadan, T.K. Peltonen, A.T. Markkola, J.I. Tanttu, J. Jääskeläinen, A.-M. Häkkinen, and R. Sepponen. 3D spin-lock imaging of human gliomas. *Magn. Reson. Imaging*, 17:1001–1010, 1999.

[76] A.J. Wheaton, A. Borthakur, M. Corbo, S.R. Charagundla, and R. Reddy. Method for reduced SAR $T_{1\rho}$-weighted MRI. *Magn. Reson. Med.*, 51:1096–1102, 2004.

[77] F. Noack. NMR field-cycling spectroscopy: Principles and applications. *Progr. NMR Spectrosc.*, 18:171–276, 1986.

[78] N.I. Matter, G.C. Scott, T. Grafendorfer, A. Macovski, and S.M. Conolly. Rapid polarizing field cycling in magnetic resonance imaging. *IEEE Trans. Med. Imaging*, 25:84–93, 2006.

[79] P.L. Volegov, J.C. Mosher, M.A. Espy, and R.H. Kraus. On concomitant gradients in low-field MRI. *J. Magn. Reson.*, 175:103–113, 2005.

[80] W.R. Myers, M. Mößle, and J. Clarke. Correction of concomitant gradient artifacts in experimental microtesla MRI. *J. Magn. Reson.*, 177:274–284, 2005.

[81] J.O. Nieminen and R.J. Ilmoniemi. Solving the problem of concomitant gradients in ultra-low-field MRI. *J. Magn. Reson.*, 207:213–219, 2010.

[82] U.S. Department of Health and Human Services, Food and Drug Administration, Center for Devices and Radiological Health. Guidance for the submission of premarket notifications for magnetic resonance diagnostic devices. Technical report, 1998.

[83] D.J. Schaefer, J.D. Bourland, and J.A. Nyenhuis. Review of patient safety in time-varying gradient fields. *J. Magn. Reson. Imaging*, 12:20–29, 2000.

[84] R. Kimmich and E. Anoardo. Field-cycling NMR relaxometry. *Progr. NMR Spectrosc.*, 44:257–320, 2004.

[85] W. Myers, D. Slichter, M. Hatridge, S. Busch, M. Mößle, R. McDermott, A. Trabesinger, and J. Clarke. Calculated signal-to-noise ratio of MRI detected with SQUIDs and Faraday detectors in fields from 10 μT to 1.5 T. *J. Magn. Reson.*, 186:182–192, 2007.

[86] K.M. Gilbert, W.B. Handler, T.J. Scholl, J.W. Odegaard, and B.A. Chronik. Design of field-cycled magnetic resonance systems for small animal imaging. *Phys. Med. Biol.*, 51:2825–2841, 2006.

[87] P. Volegov, A.N. Matlashov, M.A. Espy, J.S. George, and R.H. Kraus Jr. Simultaneous magnetoencephalography and SQUID detected nuclear MR in microtesla magnetic fields. *Magn. Reson. Med*, 52:467–470, 2004.

[88] P.E. Magnelind, J.J. Gomez, A.N. Matlashov, T. Owens, J.H. Sandin, P.L. Volegov, and M.A. Espy. Co-registration of interleaved MEG and ULF MRI using a 7 Channel low-T_c SQUID system. *IEEE Trans. Appl. Supercond.*, 21:456–460, 2011.

[89] P.A. Bandettini, N. Petridou, and J. Bodurka. Direct detection of neuronal activity with MRI: Fantasy, possibility, or reality? *Appl. Magn. Reson.*, 29:65–88, 2005.

[90] R.H. Kraus, Jr., M.A. Espy, P.L. Volegov, A.N. Matlachov, J.C. Mosher, A.V. Urbaitis, and V.S. Zotev. Toward SQUID-based direct measurement of neural currents by nuclear magnetic resonance. *IEEE Trans. Appl. Supercond.*, 17:854–857, 2007.

[91] R.H. Kraus, Jr., P. Volegov, A. Matlachov, and M. Espy. Toward direct neural current imaging by resonant mechanisms at ultra-low field. *NeuroImage*, 39:310–317, 2008.

[92] A.M. Cassará, B. Maraviglia, S. Hartwig, L. Trahms, and M. Burghoff. Neuronal current detection with low-field magnetic resonance: simulations and methods. *Magn. Reson. Imaging*, 27:1131–1139, 2009.

[93] M. Burghoff, H.-H. Albrecht, S. Hartwig, I. Hilschenz, R. Körber, N. Höfner, H.-J. Scheer, J. Voigt, L. Trahms, and G. Curio. On the feasibility of neurocurrent imaging by low-field nuclear magnetic resonance. *Appl. Phys. Lett.*, 96:233701, 2010.

[94] S. Busch, M. Hatridge, M. Mößle, W. Myers, T. Wong, M. Mück, K. Chew, K. Kuchinsky, J. Simko, and J. Clarke. Measurements of T_1-relaxation in ex vivo prostate tissue at 132 μT. *Magn. Reson. Med.*, 67:1138–1145, 2012.

[95] S.-H. Liao, K.-W. Huang, H.-C. Yang, C.-T. Yen, M.J. Chen, H.-H. Chen, H.-E. Horng, and S.Y. Yang. Characterization of tumors using high-T_c superconducting quantum interference device-detected nuclear magnetic resonance and imaging. *Appl. Phys. Lett.*, 97:263701, 2010.

[96] M. Espy, M. Flynn, J. Gomez, C. Hanson, R. Kraus, P. Magnelind, K. Maskaly, A. Matlashov, S. Newman, T. Owens, M. Peters, H. Sandin, I. Savukov, L. Schultz, A. Urbaitis, P. Volegov, and V. Zotev. Ultra-low-field MRI for the detection of liquid explosives. *Supercond. Sci. Technol.*, 23:034023, 2010.

[97] P.E. Magnelind, A.N. Matlashov, P.L. Volegov, and M.A. Espy. Ultra-low field NMR of UF_6 for ^{235}U detection and characterization. *IEEE Trans. Appl. Supercond.*, 19:816–818, 2009.

[98] D.S. van Zyl. SQUID detected low-field NMR for the evaluation of internal fruit quality. Master's thesis, Stellenbosch University, South Africa. 2010.

[99] D. Cohen. Magnetoencephalography: evidence of magnetic fields produced by alpha-rhythm currents. *Science*, 161:784–786, 1968.

[100] F. Öisjöen, J.F. Schneiderman, G.A. Figueras, M.L. Chukharkin, A. Kalabukhov, A. Hedström, M. Elam, and D. Winkler. High-T_c superconducting quantum interference device recordings of spontaneous brain activity: Towards high-T_c magnetoencephalography. *Appl. Phys. Lett.*, 100:132601, 2012.

[101] H. Xia, A. Ben-Amar Baranga, D. Hoffman, and M.V. Romalis. Magnetoencephalography with an atomic magnetometer. *Appl. Phys. Lett.*, 89:211104, 2006.

[102] J.P. Mäkelä, N. Forss, J. Jääskeläinen, E. Kirveskari, A. Korvenoja, and R. Paetau. Magnetoencephalograhy in neurosurgery. *Neurosurgery*, 59:493–510, 2006.

[103] F. de Pasquale, S. Della Penna, A.Z. Snyder, C. Lewis, D. Mantini, L. Marzetti, P. Belardinelli, L. Ciancetta, V. Pizzella, G.L. Romani, and M. Corbetta. Temporal dynamics of spontaneous MEG activity in brain networks. *Proc. Natl. Acad. Sci. USA*, 107:6040–6045, 2010.

[104] M. van Gerven and O. Jensen. Attention modulations of posterior alpha as a control signal for two-dimensional brain–computer interfaces. *J. Neurosci. Methods*, 179:78–84, 2009.

[105] N. Neumann, A.M. Dubischar-Krivec, C. Braun, A. Löw, F. Poustka, S. Bölte, and N. Birbaumer. The mind of the mnemonists: An MEG and neuropsychological study of autistic memory savants. *Behav. Brain. Res.*, 215:114–121, 2010.

[106] R. Salmelin. Clinical neurophysiology of language: The MEG approach. *Clin. Neurophys.*, 118:237–254, 2007.

[107] J.C. Mosher, P.S. Lewis, and R.M. Leahy. Multiple dipole modeling and localization from spatio-temporal MEG data. *IEEE Trans. Biomed. Eng.*, 39:541–557, 1992.

[108] M.S. Hämäläinen and R.J. Ilmoniemi. Interpreting measured magnetic fields of the brain: estimates of current distributions, Report TKK-F-A559, Helsinki University of Technology, Finland. 1984.

[109] M.S. Hämäläinen and R.J. Ilmoniemi. Interpreting magnetic fields of the brain: minimum norm estimates. *Med. Biol. Eng. Comput.*, 32:35–42, 1994.

[110] A. Dale and M. Sereno. Improved localization of cortical activity by combining EEG and MEG with MRI cortical surface reconstruction: a linear approach. *J. Cogn. Neurosci.*, 5:162–176, 1993.

[111] P.T. Vesanen, J.O. Nieminen, K.C.J. Zevenhoven, J. Dabek, J. Luomahaara, J. Hassel, J. Penttilä, A.V. Zhdanov, F.-H. Lin, L.T. Parkkonen Y.-C. Hsu, J. Simola, A.I. Ahonen, and R.J. Ilmoniemi. A 72-channel whole-head system for combined ultra-low-field MRI and magnetoencephalography. *In Proc. Intl. Soc. Magn. Reson. Med.*, page 2745, 2012.

[112] S. Hartwig, J. Voigt, H.-J. Scheer, H.-H. Albrecht, M. Burghoff, and L. Trahms. Nuclear magnetic relaxation in water revisited. *J. Chem. Phys.*, 135:054201, 2011.

[113] J.R. Zimmermann and W.E. Brittin. Nuclear magnetic resonance studies in multiple phase systems: lifetime of a water molecule in an adsorbing phase on silica gel. *J. Phys. Chem.*, 61:1328–1333, 1957.

[114] Y.S. Greenberg. Application of superconducting quantum interference devices to nuclear magnetic resonance. *Rev. Mod. Phys.*, 70:175–222, 1998.

[115] M.A. Uusitalo and R.J. Ilmoniemi. Signal-space projection method for separating MEG or EEG into components. *Med. Biol. Eng. Comput.*, 35:135–140, 1997.

[116] R.D. Venook, N.I. Matter, M. Ramachandran, S.E. Ungersma, G.E. Gold, N.J. Giori, A. Macovski, G.C. Scott, and S.M. Conolly. Prepolarized magnetic resonance imaging around metal orthopedic implants. *Magn. Reson. Med.*, 56:177–186, 2006.

[117] M.E. Halse, A. Coy, R. Dykstra, C. Eccles, M. Hunter, R. Ward, and P.T. Callaghan. A practical and flexible implementation of 3D MRI in the Earth's magnetic field. *J. Magn. Reson.*, 182:75–83, 2006.

[118] E. Niedermeyer and F. Lopes da Silva. *Electroencephalography: Basic Principles, Clinical Applications, and Related Fields*. Lippincott Williams & Williams, Philadelphia, USA, 2005.

[119] R.J. Ilmoniemi, J. Ruohonen, and J. Karhu. Transcranial magnetic stimulation—a new tool for functional imaging of the brain. *Crit. Rev. Biomed. Eng.*, 27:241–284, 1999.

Aalto-DD 87/2013

ISBN 978-952-60-5177-2
ISBN 978-952-60-5178-9 (pdf)
ISSN-L 1799-4934
ISSN 1799-4934
ISSN 1799-4942 (pdf)

Aalto University
School of Science
Department of Biomedical Engineering and Computational Science

BUSINESS + ECONOMY

ART + DESIGN + ARCHITECTURE

SCIENCE + TECHNOLOGY

CROSSOVER

DOCTORAL DISSERTATIONS